Synthesis, characterization and excited state dynamics of $Cs_4CuSb_2Cl_{12}$ double perovskite

A dissertation submitted for the partial fulfilment

of the BS-MS Dual Degree

in

CHEMICAL SCIENCES

by

Shradha Sapru

MS16034

at

Indian Institute of Science Education and Research (IISER) Mohali

April 2021

CERTIFICATE OF EXAMINATION

This is to certify that the dissertation titled "**Synthesis, characterization and excited state dynamics of $Cs_4CuSb_2Cl_{12}$ double perovskite"** submitted by **Ms. Shradha Sapru** (Reg. No. MS16034) for the partial fulfilment of the BS-MS dual degree programme of the Institute, has been examined by the thesis committee duly appointed by the Institute. The committee finds the work done by the candidate satisfactory and recommends that the report be accepted.

Dr. Ujjal Gautam	Dr. Sanchita Sengupta	Dr. Arijit Kumar De
		(Supervisor)

Date: April 26, 2021

DECLARATION

The work presented in this dissertation has been carried out by me under the guidance of Dr. Arijit Kumar De at the Indian Institute of Science Education and Research Mohali.

This work has not been submitted in part or in full for a degree, a diploma, or a fellowship to any other university or institute. Whenever contributions of others are involved, every effort is made to indicate this clearly, with due acknowledgement of collaborative research and discussions. This thesis is a bonafide record of original work done by me and all sources listed within have been detailed in the bibliography.

Shradha Sapru

(Candidate)

Date: April 26, 2021

In my capacity as the supervisor of the candidate's project work, I certify that the above statements by the candidate are true to the best of my knowledge.

Dr. Arijit Kumar De

(Supervisor)

ACKNOWLEDGEMENTS

First of all, I would like to thank Dr. Arijit Kumar De, my Master's thesis supervisor, for his constant support and guidance throughout the course of my project. My interactions with him have helped me develop great insights and understand my project better. Working in his lab has provided me with a hands-on experience and exposure to a myriad of experimental tools and techniques. He has been very generous, understanding and supportive throughout the pandemic.

I would also like to express my gratitude to my committee members, Dr. Ujjal Gautam and Dr. Sanchita Sengupta for their valuable inputs and suggestions to make this research more accurate and comprehensive.

I would like to specially thank Ms. Samita Mishra for giving my project a direction, teaching me various techniques and guiding me from the very beginning. She has been a great mentor and her training has equipped me with several experimental skills. Her dedication and enthusiasm have made this work possible.

I am grateful to every lab member of the "Condensed Phase Dynamics" group, Dr. Subhash Chander, Dr. Anita Yadav, Dr. Anita Devi, Ms. Yogita Silori, Ms. Shaina Dhamija, Mr. Sumit Yadav, Ms. Garima Bhutani, Ms. Sakshi Chawla, Mr. Subho Mitra, Mr. Ajay Jayachandran and Ms. Mansi Kothari for their support, inspiration and fruitful discussions.

I would like to thank IISER Mohali for all the instrumentation facilities and the library for providing access to a plethora of journals.

Finally, I am eternally grateful to my parents, Mr. Sunil Sapru and Mrs. Meenakshi Sapru, my sister, Ms. Shraya Sapru and my dearest friends Ardra, Ruchira, Soumya, Puneeth, Sasank, Mayank bhaiya and Manisha for their constant love, motivation and encouragement. I would not have been able to accomplish all of this without their support.

CONTENTS

LIST OF FIGURES

LIST OF TABLES

ABBREVIATIONS

BBO	Beta Barium Borate (BaB_2O_4)
CBM	Conduction band minima
CCSC	$Cs_4CuSb_2Cl_{12}$
CIGS	Copper indium gallium selenide
DFT	Density functional theory
DOS	Density of states
DP	Double perovskite
DSSC	Dye-sensitised solar cells
EPR	Electron paramagnetic resonance
ESA	Excited State Absorption
ETL	Electron transport layer
FTO	Fluorine doped tin oxide
GSB	Ground State Bleach
HCSC	Hot carrier solar cell
HOIP	Hybrid organic-inorganic perovskite
HR-XPS	High resolution-X-ray photoelectron spectroscopy
HTL	Hole transport layer
ITO	Indium doped tin oxide
LED	Light emitting diode
MA	Methylammonium cation
MC	Microcrystal

MHP	Metal halide perovskite
NC	Nanocrystal
NOPA	Noncollinear Optical Parametric Amplifier
P3HT	poly(3-hexylthiophene-2,5-diyl)
PBE	Perdew, Burke and Ernzerhof
PCBM	phenyl-C61-butyric acid methyl ester
PCE	Power conversion efficiency
PIA	Photo-induced absorption
PL	Photoluminescence
PV	Photovoltaic
SE	Stimulated Emission
SQ	Shockley-Queisser
Spiro-OMeTAD	2,2$^{'}$,7,7$^{'}$-Tetrakis[N,N-di(4-methoxyphenyl)amino]-9,spirobifluorene
TAS	Transient absorption spectroscopy
TCO	Transparent conducting oxide
UPS	Ultraviolet photoelectron spectroscopy
VBM	Valence band maxima
XPS	X-ray photoelectron spectroscopy

ABSTRACT

Metal halide perovskites have recently emerged as one of the fastest growing photovoltaics technology. In the span of a decade, the efficiencies of these solar cells have increased from a mere 3.8% to 25.5%. Perovskite solar cells have developed as a technology with competitive efficiency values, facile synthesis methods and great potential, to either replace or be used in conjunction with silicon solar cells. In this respect, the most successful candidates are the lead halide perovskites, in particular, methylammonium lead triiodide ($MAPbI_3$). Despite this progress, these hybrid organic-inorganic lead halide perovskites have stability and toxicity issues. The film is sensitive to humidity and oxygen, the organic cations are volatile and lead ions are toxic in nature. Hence, there is a need to develop non-toxic alternatives to lead halide perovskites, and improve their stability and efficiency for solar cell applications.

The recent development of double perovskites has proven as a viable alternative to lead halide perovskites. One of the materials gaining importance in this respect is the $Cs_4CuSb_2Cl_{12}$ (CCSC) double perovskite. CCSC has exhibited high photo- and thermal-stability, is tolerant to humidity and has a suitable bandgap. This makes CCSC a potential candidate to be used as an absorber material in solar cells. However, to better comprehend the utility of this material, it is important to understand the nature of its bandgap and its excited state dynamics. Here, we have synthesized the microcrystals of CCSC, investigated its band structure and using femtosecond transient absorption spectroscopy, we have explored the relaxation rates and pathways of hot-carriers in this material. An understanding of the hot carrier relaxation process in CCSC is essential to gain valuable information on its intrinsic carrier dynamics and applications for the development of hot carrier solar cells.

Chapter-1

Perovskites: An emerging photovoltaics technology

1.1. Introduction

Energy production is one of the basic requirements for the sustenance of mankind on earth. Energy is required for transportation, residential, industrial and commercial purposes. As the world population keeps increasing, energy consumption is only bound to increase in the coming years. Our global energy need at present is about 15 TW.[1] Nearly 81% of this energy comes from fossil fuels, 16% from renewable energy resources (with a major contribution from biomass) and about 3% from nuclear energy (Figure 1.1).[2]

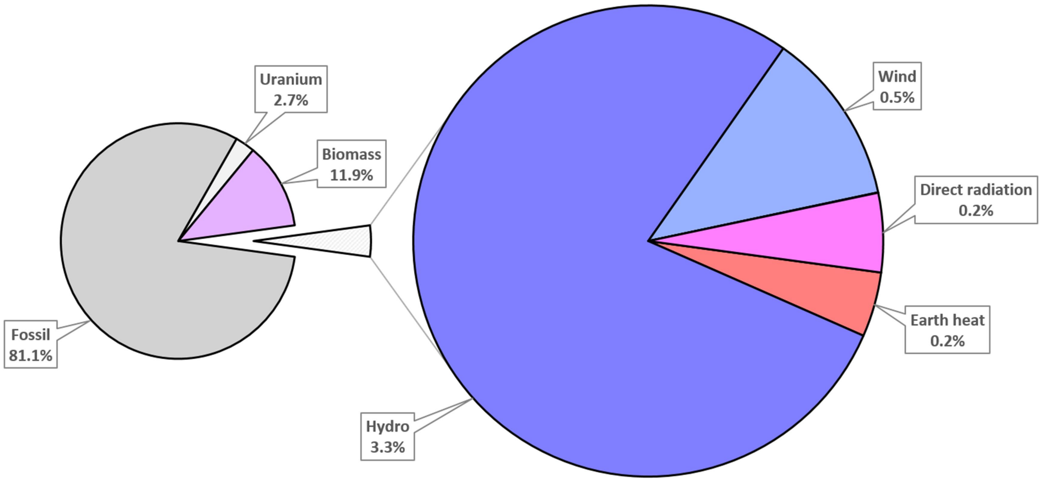

Figure 1.1. *Contribution of different sources to our energy consumption.*[2]

Worldwide, fossil fuels form the major energy source which has been used for more than a century to help meet our ever-increasing energy demands. This involves burning of fuels such as coal, petroleum and natural gas in order to obtain energy for our day-to-day activities. Fossil fuels are obtained from the dead remains of plants and animals which have been compressed and decomposed over millions of years. However, the current rate at which this resource is being consumed far exceeds the rate of its production. Hence, they are non-renewable sources of energy. In addition to this, burning of these fuels results in the release of toxic gases such as sulphur dioxide, nitrogen oxides, volatile organic compounds etc., thus contributing to environmental pollution. These fuels are also majorly responsible for releasing CO_2 into our atmosphere, further adding to the growing concerns of global warming.[2] These reasons have propelled the urgent need for eco-friendly and renewable alternatives to fossil fuels. While nuclear energy is a strong contender to renewable energy sources, the radioactive waste left from its use and the sheer danger that nuclear power plants pose, has limited its utility.[3] Over the past few years, greater attention has been drawn towards solar, wind and water as sources of energy generation.

Figure 1.2 shows a comparison in terms of the total amount of energy available from different sources. Out of the renewable sources of energy, wind is the most abundant in terms of its availability (after sunlight), and only a small portion of energy is available from hydro-power. However, at present, hydro-power is more widely used as compared to wind energy. This means that a much larger proportion of our available water resources have already been put to use for obtaining energy, while a large part of the wind resources remain untapped. In comparison to these renewable energy sources, there is a large availability of fossils and uranium reserves, which would be sufficient to meet our energy demands for several years to come. This however, doesn't rule out the environmental impact of the use of fossil fuels. Additionally, the total amount of fossil fuels available for use will eventually decrease with every passing year, while renewable energy resources replenish every year and hence would remain nearly constant.[2,4,5]

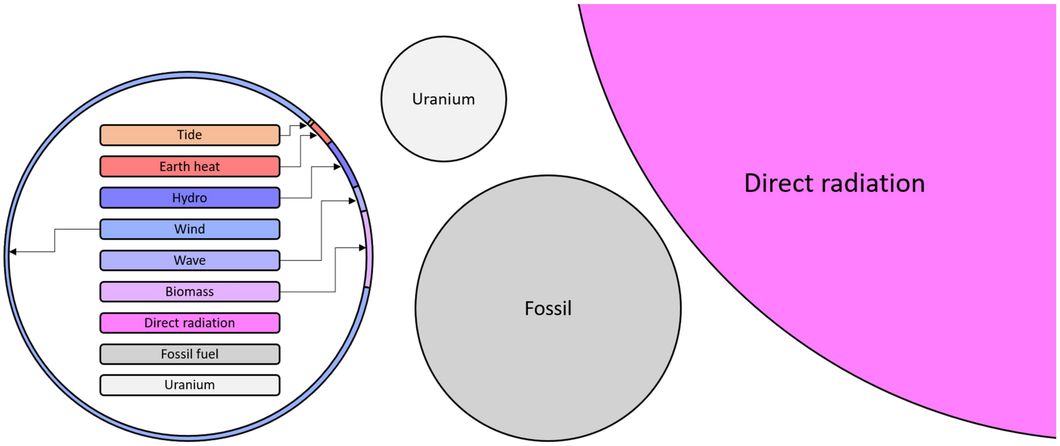

Figure 1.2. *Proportion of energy available from different sources.*[4]

In contrast to all other sources of energy, solar energy appears to be the most promising energy source due to its sheer abundance, which overshadows the available reserves of fossil fuels, nuclear as well as other renewable energy sources. The amount of energy from sunlight absorbed by the atmosphere in one hour is sufficient to meet the world's energy demands for an entire year. Solar energy offers relatively easy strategies to convert light to electricity. This results in sunlight having the maximum potential to meet our energy demands, with a need for greater focus on harnessing this energy in order to attain the maximum output.[6]

1.2. Emergence of photovoltaics

The field of photovoltaics emerged with the discovery of the photovoltaic effect by Alexandre Edmond Becquerel in 1839.[7] He observed that on illuminating platinum electrodes immersed in an electrolyte, current and voltage were generated and this was directly related to the strength of the illumination. This was followed by Willoughby Smith's observation of photoconductivity in selenium in 1873. The photovoltaic (PV) effect was discovered in an all solid-state material for the first time by William Grylls Adams and his student, Richard Evans Day in 1877, where they observed the generation of current on irradiating the junction of selenium and platinum with light.[8] Eventually, the development of the first selenium-based solar cells took place in 1883 by Charles Fritts, which had a power conversion efficiency of 1%.[9] Though at this stage photovoltaics seemed to be a very promising energy source, there wasn't enough knowledge in terms of the mechanism which led to the observed behaviour. In addition to this, the use of fossil fuels gradually increased with a greater ease of extraction of energy.

In 1905 a theoretical understanding of this phenomenon was provided by Albert Einstein, known as the photoelectric effect, which led him to win the Nobel Prize in Physics in 1921. The practical applications of solar cells came into effect with the discovery of the silicon p-n junction in 1941 by Russell Shoemaker Ohl. Studies in the Bell Laboratories by Gerald L. Pearson, Daryl M. Chapin and Calvin S. Fuller in the 1950s further led to the development of silicon solar cells, thus boosting the field of photovoltaics.[10] The major drawback of this technology was that it was extremely expensive to be used for commercial purposes. While efforts were ongoing to make this technology feasible for practical use, the space race in the 1950s and 1960s tremendously boosted the use of solar cells for space applications. Solar cells began to be extensively used in space crafts and satellites, as it was economically more feasible to have power being generated from these cells in comparison to the stored energy from battery systems. Advancements in this front led to a switch from silicon solar cells to gallium arsenide (GaAs) for space applications, in the 1990s. The efficiency offered by GaAs solar cells is much greater than that of the traditional silicon solar cells and this gave rise to the development of the thin-film solar cell technology.[11]

In 1961, a study by William Shockley and Hans-Joachim Queisser established the maximum theoretical efficiency of a p-n junction solar cell with a 1.1 eV bandgap as

30%.[12] Among other assumptions, this model assumed radiative recombination as the only mechanism for energy loss in the solar cell. Using a global solar spectra and a back surface mirror, the maximum efficiency limit for a solar cell with 1.34 eV bandgap was increased to 33.7%.[13] This value is known as the Shockley-Queisser (SQ) limit. Since then, efforts are ongoing to exploit the existing PV technologies in order to reach as close as possible to this theoretical limit.

1.2.1. Different generations of solar cells

Over the years, with the growth of the photovoltaics industry, solar cells have been segregated into different generations based on the timeline of their discovery and type of technology (Figure 1.3).[14] The traditional crystalline silicon wafer solar cell technology forms the first generation of solar cells. The rooftop solar panels are made of these cells. Their efficiency values have increased to 26% over the years (Figure 1.4).[15] Silicon solar cells can be either monocrystalline or polycrystalline in nature. Monocrystalline silicon solar cells are produced from a single crystal of silicon, whereas polycrystalline silicon solar cells are made from multiple silicon fragments melted together. The efficiency of monocrystalline silicon solar panels is relatively higher than that of the polycrystalline one, but their production is more energy consuming in nature. Silicon solar cells have been successful due to the abundance of the raw material, suitable band gap (towards the lower side of the solar spectrum), moderate to good power conversion efficiency (PCE) values and their longevity. However, their major drawback is their long energy payback time. Energy payback time refers to the number of years it takes for a solar power plant to regain energy that has been consumed during the production of the solar cells. In this respect, developing silicon solar panels is an energy intensive process and its energy payback time ranges from one to four years depending on the method of production and location of installation of the plant. Additionally, their manufacturing process is costly and the cells are heavy and rigid.[16]

The second generation of photovoltaic cells is known as the thin-film solar cell technology. These cells were developed to overcome the drawbacks of the first generation of solar cells in terms of their rigidity and expensive manufacturing process. Solar cells in this category are usually a few micrometers thick (hence referred to as thin films), resulting in light-weight and flexible photovoltaic devices.[17] Amorphous silicon, cadmium telluride (CdTe) and copper indium gallium selenide (CIGS) form a part of this generation of devices. Production of amorphous silicon is easier as compared to crystalline silicon, but the film is unstable and the device has a low PCE. CdTe and CIGS have an optimal band gap, between 1.2-1.7 eV, which covers a wide range of the solar spectrum and have attained efficiencies of 22%.[15] However, these solar cells utilise metals with low abundance which are heavy and toxic, thus raising serious concerns in terms of scalability of this technology. The production of these cells also results in the consumption of large amounts of energy, they have lower efficiencies as compared to the first generation of solar cells and their production costs are also higher.[18,19]

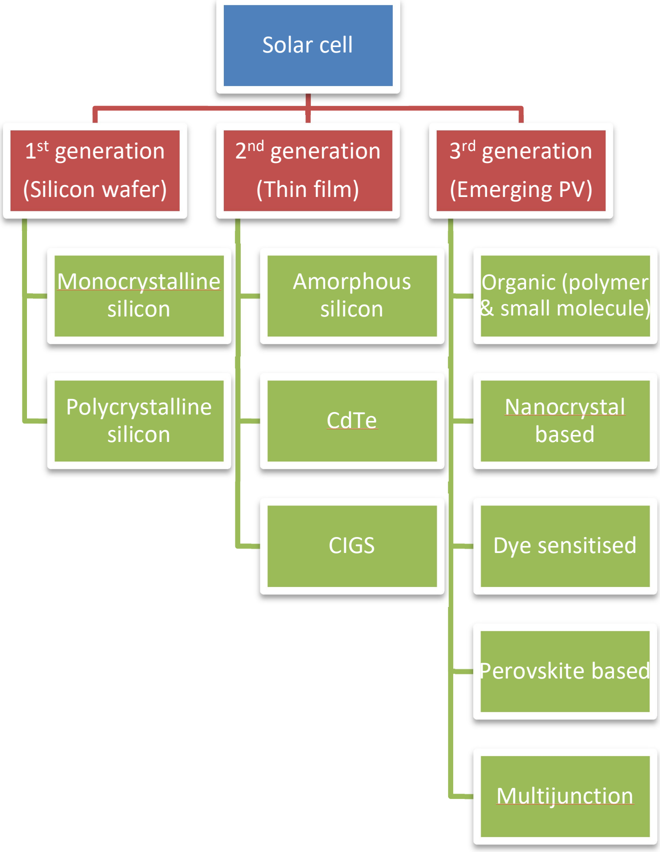

Figure 1.3. *Different generations of solar cells.*[14]

The third generation of solar cells refers to the emerging photovoltaic technologies which aim to be inexpensive in manufacturing, along with offering good efficiency values and easy synthesis methods. This generation includes dye-sensitised, organic, multijunction, nanocrystals-based and perovskite solar cells.[20,21] These materials have the potential to exceed the conventional Shockley-Queisser limit of 33% for single junction solar cells, due to their unique structure and inherent properties. In this regard, multijunction solar cells are the most efficient. These cells consist of two to four layers of different semiconductor materials whose band gaps are complimentary to each other in a way that covers a major portion of the solar spectrum. This ensures greater absorption of the sun's radiation and in turn, more efficient devices.[22] However, these devices are extremely expensive to manufacture and hence are mainly employed for space applications. Organic solar cells (polymer and small molecule) are easy to manufacture, inexpensive and light-weight, but have low PCEs. Dye-sensitised solar cells have a low-cost manufacturing process, abundant raw materials and are semi-transparent with applications for being used in buildings. These cells, however, utilise dyes which photo bleach and hence are not durable, use electrolyte solutions containing volatile organic compounds which hazardous to human health, and have low efficiency values. Perovskite solar cells offer a variety of advantages as they are solution-processable and hence are easy to manufacture, have a tunable band gap, low production cost and use earth-abundant elements.[20,21] They have some issues related to their stability and toxicity; however, there have been advances in the recent past to mitigate these concerns. In addition to overcoming the drawbacks of other solar cell technologies, perovskite solar cells have achieved good power conversion efficiencies as well.[15] These factors have led to the recent popularity of this material. A detailed discussion on perovskites is given later in this chapter (Section 1.3).

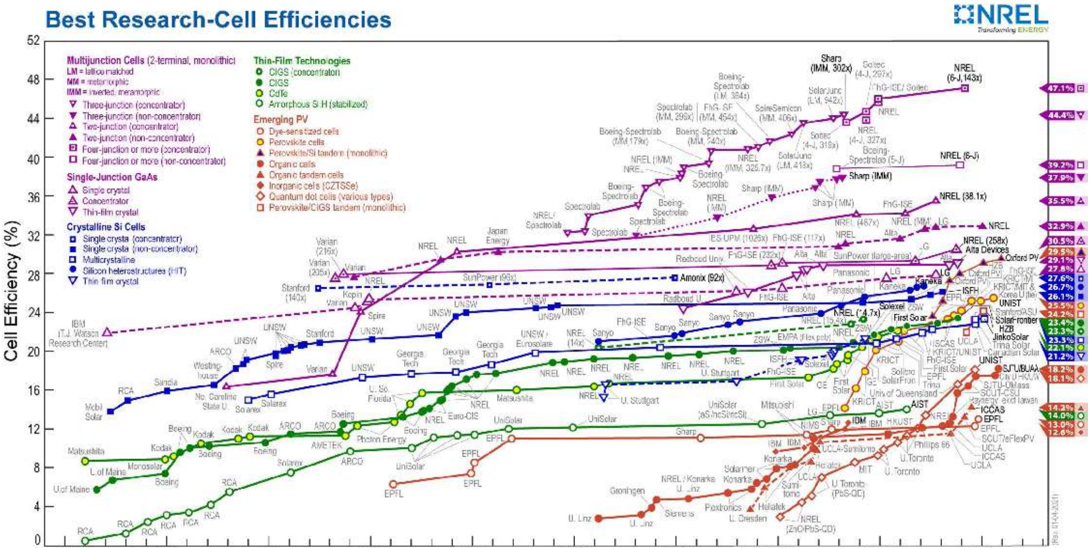

Figure 1.4. *Best research cell efficiencies of different photovoltaic technologies.*[15]

Figure 1.4 depicts the enhancement in PCEs of different solar cell technologies over a period of ~50 years as given by NREL.[15] Crystalline Si solar cells, with a PCE of 26.7%, have maintained their position over the years and still remain the most widely deployed technology for terrestrial use. The highest efficiency of 47.1% till date has been obtained from multijunction solar cells (six-junction).[23] Some of these devices deploy concentrator systems for enhancing their efficiency. This refers to the utilisation of more than one sun as the illuminating source and thus results in higher PCEs due to higher intensity of sunlight. However, this would not be very useful for practical applications. As evident from Figure 1.4, perovskite solar cells have emerged as the fastest growing photovoltaics technology in the recent past. Over the span of a decade, this technology has progressed to achieve comparable or exceed the efficiency values obtained from other thin film technologies on which research has been going on for more than 40 years.

The first paper to report the use of perovskites in solar cells was by Miyasaka et. al. in 2009, where the perovskite material was used as a sensitiser layer in a structure similar to the DSSC.[24] Over the past decade, there has been a rapid increase in the PCE of perovskite based solar cells.[25] From a mere 3.8% efficiency in the DSSC in 2009,[24] to 10.8% in the solid-state DSSC,[26] the PCE of perovskite solar cells is currently at 25.5%. Metal halide perovskites have already far exceeded the PCE obtained from DSSCs (13.0%), amorphous silicon (14.0%) and organic solar cells (18.2%).[15] Though their efficiency is slightly lower than that of crystalline silicon at present, perovskite-silicon tandem solar cells stand at a PCE of 29.5%, which are on the path of commercialisation by Oxford PV.[15] This exceeds the efficiency of the traditional silicon cells and is bound to increase in the coming years. With rapid advancements in research on perovskites, and with the development of perovskite-silicon and all-perovskite tandem solar cells, perovskites have the potential to either replace or be used in conjunction with other solar cell technologies for terrestrial applications. There is a need to understand their structure, properties and intrinsic dynamics in order to exploit them for use in the photovoltaics industry.

1.3. Perovskites

The term "perovskite" refers to a class of compounds with the chemical formula of ABX_3. The traditional perovskites have a cubic crystal structure, with cation A occupying the corner sites, cation B occupying the body centre and anion X occupying the face centre (Figure 5(a)). It can also be understood as an ion A occupying the vacant sites between layers of BX_6 octahedra, where X form the corner sharing ions (Figure 5(b)). The first perovskite, calcium titanate ($CaTiO_3$), was discovered by the German mineralogist Gustav

Rose in 1839, and was named after the Russian mineralogist Lev Perovski.[27] Since then, perovskites have been widely studied. However, their applications in optoelectronics and photovoltaics, for example, light emitting diodes (LEDs), solar cells and lasers has only recently been extensively researched.[28,29] Metal halide perovskites form the basis of perovskite solar cells, with $MAPbX_3$ being one of the most common and successful candidates.[24,26] Here, the A site is occupied by the methyl ammonium (MA) cation, B site is occupied by Pb^{2+} and X represents the halide ions (Cl^-, Br^-, I^-).

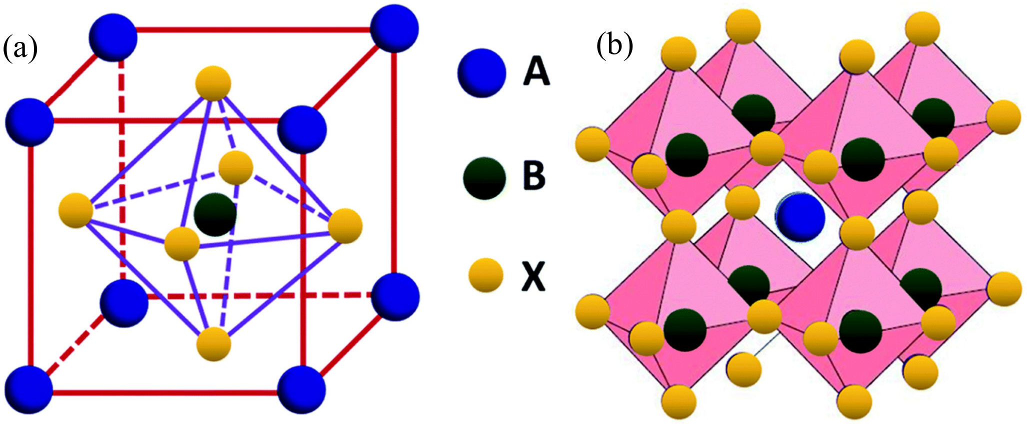

Figure 1.5. *(a) Cubic crystal structure of a typical ABX_3 type perovskite (b) Extended three-dimensional structure with corner sharing X ions.*[30]

1.3.1. Properties of metal halide perovskites

Metal halide perovskites (MHPs), be it hybrid organic-inorganic perovskites (HOIP) or all-inorganic perovskites, can be prepared through low-temperature solution processable methods (facile synthesis), are inexpensive to manufacture and utilise earth abundant elements.[31,32] These properties, in addition to being lightweight, flexible and semi-transparent, have resulted in the commercialisation of this technology.[28] Depending on the temperature and the size of the organic/inorganic cations present in the perovskite, this material can have a cubic, tetragonal or orthorhombic crystal structure.[33] MHPs have a high absorption coefficient, which aids the synthesis of thin films, with a thickness much lower than their diffusion lengths.[28,34] This results in efficient charge carrier formation and separation.[32] An exchange or use of mixed halide ions helps in adjusting the bandgap in the UV-Visible-Near IR region.[35] This allows tuning of their photoluminescence (PL),[36] with emissions spanning the entire visible range and they have high PL quantum yields as well.[37] Depending on the perovskite material and whether it is a single crystal or polycrystalline in nature has resulted in different trap densities being obtained. Irrespective of the trap densities, perovskites in general, are more defect tolerant as compared to other semiconductor technologies.[38,39]

$MAPbI_3$, the most commonly used solar cell absorber, has an experimentally obtained direct bandgap value of ~1.6 eV.[34] It has low hole and electron effective masses comparable to that of inorganic semiconductors, with moderate charge carrier mobility.[40,41] This moderate carrier mobility has been attributed to lattice fluctuations, such as phonon scattering and polaron formation.[42] Efficient carrier collection in these HOIPs is possible due to their long carrier lifetimes and long diffusion lengths.[29,43] These properties make $MAPbI_3$ one of the best absorber materials to be used in solar cells. The reason for the success of lead in these perovskites has been attributed to its antibonding $6s^2$ valence shell which forms the valence band maxima, and the 3D network of $[PbI_6]^{4-}$ octahedra formed which corner sharing I^- ions.[44] These materials have the potential to overtake the existing solar cell technologies in addition to overcoming the issues faced by most of them.

1.3.2. Challenges to perovskite solar cells

Despite the range of properties displayed by lead halide perovskites, there remain two major concerns that limit the use of these materials at the commercial level – toxicity and low stability.[45,46] The use of lead in perovskite solar cells poses an environmental and health hazard. Efforts are ongoing to overcome this, by replacing lead with other divalent ions or a combination of cations, leading to double perovskites.

Lead halide perovskites, in particular $MAPbI_3$, are sensitive to excessive exposure to moisture,[45,47] light or oxygen[48] and high temperatures.[48,49] When these factors are combined together, it results in a rapid degradation of the perovskite film.[47] Organic cations used at the A site are hygroscopic and volatile in nature and can result in an irreversible degradation of the perovskite film.[45] In addition to degradation of perovskites under exposure to strong UV radiation, the most commonly used ETL, TiO_2, is also highly sensitive to UV rays.[45] It has been observed that in an oxygen-rich atmosphere, the perovskite tends to form structures of PbI_2, resulting in inhomogeneity.[48] Apart from the above extrinsic factors, intrinsic factors such as formation of defects during the synthesis of perovskite thin films also contribute to their instability. Vacancies within the crystal lattice result in ion and hole migration.[50] Ion migration deteriorates the PCE of the perovskite solar cell and also creates a local electric field, which further decreases its efficiency.[47]

To overcome these limitations, different strategies such as encapsulation, using additives, using mixed cation or mixed anion systems have been established.[51] Encapsulating perovskite solar cells provides a great means to protect the device from UV light, oxygen and moisture.[52,53] This promotes the safe handling of lead as well. Additives such as polyethylene glycol, polyvinylpyrrolidone etc. allow uniform film growth and provide thermal stability.[54] Changing the A, B or X site ions or using a combination of ions at these sites can combat the stability issue as well as provide a wide range of bandgap values. In this direction, formamidinium (FA), cesium (Cs) or mixed cations such as, $FA_{1-x}MA_xPbI_3$ or $Cs_xMA_{1-x}PbI_3$ have been used in place of methylammonium (MA), to overcome its hygroscopic nature.[55] While choosing cations to be replaced in the perovskite structure, it is important to keep in mind that they must be large enough to perfectly fit into the vacant sites between the perovskite layers. Similarly, Sn, Ge or Sn-Pb mixtures have been used at the B site and Cl, Br or I at the X site.[56,57]

1.3.3. Alternatives to the ABX_3 type lead-based perovskite

Though lead has served as the most efficient B site cation for solar cell purposes, its toxicity limits its use. This has led to the development of lead-free perovskites. In this direction, attempts were made initially to replace Pb^{2+} with other group 14 elements such as Sn^{2+} and Ge^{2+}.[56,58] However, these perovskites had poor stability due to the easy oxidation of Sn^{2+} and Ge^{2+} to Sn^{4+} and Ge^{4+}, resulting in the loss of the essential 3D network as well.[59] Replacing Pb^{2+} with trivalent ions such as Bi^{3+} and Sb^{3+} was another strategy, which resulted in a stoichiometry and structural change due to the charge imbalance.[60,61] The perovskites obtained were of the form $A_3B_2X_9$, which were either 2D layered structures or 0D structures (Figure 1.6). Even though these perovskites were stable, this reduced dimensionality led to a decrease in the band dispersion. The $A_3B_2X_9$ type perovskites have low carrier mobility and indirect or wide bandgaps, thus making them unsuitable for photovoltaic purposes.[62,63]

An alternative strategy of substituting lead with a mixed cation system has given rise to the field of double perovskites (DPs). The introduction of DPs has opened new avenues to the development of stable, non-toxic lead-free perovskites. In one type of double perovskite system, two Pb^{2+} ions are replaced with one monovalent and one trivalent cation, resulting in the chemical formula $A_2B^IB^{III}X_6$ (A: Cs, CH_3NH_3; B^I: Cu, Ag, Au, In, K; B^{III}: Bi, Sb, In; X: Cl, Br, I).[64,65] This class of perovskites is structurally stable and maintains the conventional 3D perovskite structure. $Cs_2AgBiCl_6$ and $Cs_2AgBiBr_6$ were among the first double perovskites to be developed and displayed wide indirect bandgaps.[65,66] Post this, several DPs were reported, which either had a wide direct bandgap such as $(CH_3NH_3)_2KBiCl_6$ and $Cs_2AgInCl_6$, or an indirect bandgap such as $(CH_3NH_3)_2AgBiBr_6$ and $(CH_3NH_3)_2AgSbI_6$. Indium(I) based DPs were unstable due to the conversion of In^+ to In^{3+}.[67] Similarly, tellurium based DPs were also synthesised but are toxic in nature. Hence, despite the structural stability that DPs provide, these materials have indirect and/or wide bandgaps, which limits their use as solar cell absorbers.[68]

Recently, a new class of DPs of the form $A_4B^{II}B_2^{III}X_{12}$ (B^{II}: Cu, Mn, Cd; B^{III}: Sb, Bi) has been explored. In these DPs, four Pb^{2+} ions are replaced with one bivalent and two trivalent cations (Figure 1.6). These perovskites assume a layered monoclinic $C2/m$ crystal structure, are stable and have reported both direct and indirect bandgap values, lying in the visible range. They have suitable bandgaps, low exciton binding energy and small carrier effective mass.[69] Studies on these DPs are currently ongoing and they have the potential to overcome the issues faced by lead halide and other classes of perovskites as well.[70]

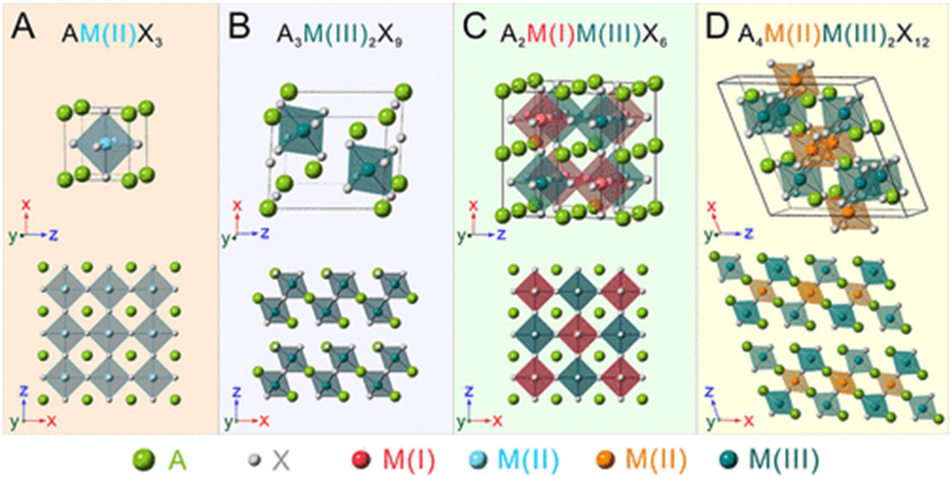

Figure 1.6. *Different types of perovskite structures.*

1.3.4. Structure of perovskite solar cells

Figure 1.7 shows the different layers comprising a perovskite solar cell. The first layer is that of a transparent electrode known as transparent conducting oxide (TCO). The most commonly used TCOs are FTO (Fluorine doped tin oxide) and ITO (Indium doped tin oxide). This layer allows sunlight to enter into the solar cell and subsequently helps in the transport of the electrons to the outer circuit. This is followed by the electron transport layer (ETL), for example TiO_2, SnO_2, In_2O_3, PCBM etc. This layer helps in the extraction of the photo-excited electrons generated within the perovskite. The next layer is of the absorber material, the perovskite, whose thickness usually ranges from a few hundred nanometers to some micrometers. On the other side of the perovskite layer is the hole transport layer (HTL), such as Sipro-OMeTAD, P3HT, NiO_x, carbon nanotubes etc. The HTL extracts and transports holes from the perovskite to the outer layers. The final layer is that of the electrode, usually Au, Ag or Al, which serves as a contact to complete the circuit.

Perovskite solar cells can be constructed in two ways. The first is the planar heterojunction, where every layer is in the solid state form. Planar heterojunctions can be developed in the n-i-p (negative-intrinsic-positive) or the p-i-n configuration. The n-i-p structure (Figure 1.7(a)) is a conventional way of constructing solar cells in which light enters through the ETL of the cell. The p-i-n structure (Figure 1.7(b)) is an inverted configuration in which light enters through the HTL.[71] The other type of perovskite solar cell has a mesoporous structure (Figure 1.7(c)), in which there is a slight modification at the junction of the ETL and the absorber layer. An additional mesoporous scaffold is present, which could be conducting or non-conducting in nature and makes a better contact with the perovskite layer. This allows for efficient extraction of electrons into the ETL and outer circuit.[72,73]

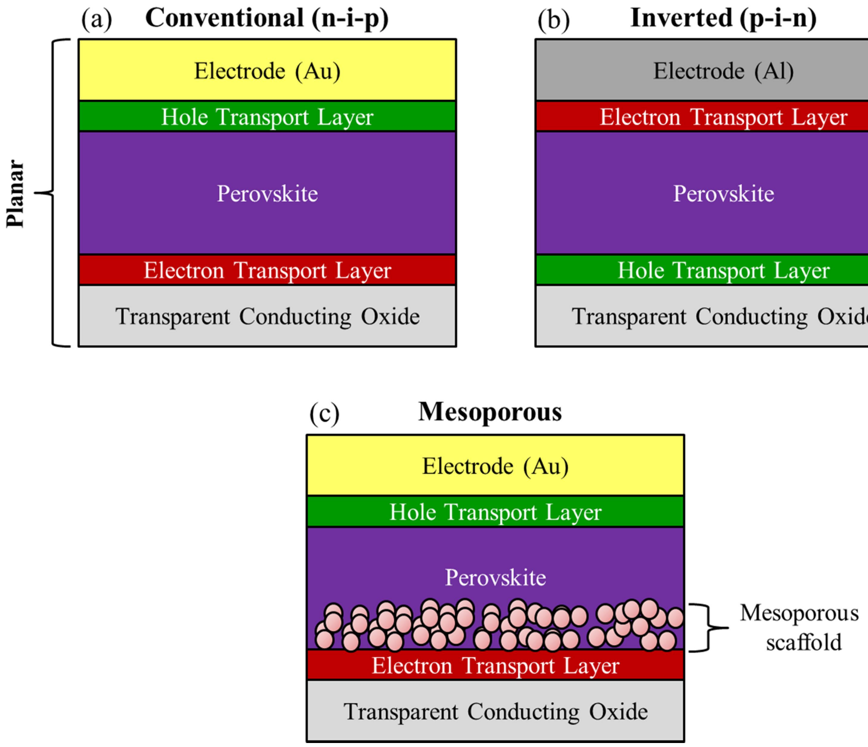

Figure 1.7. *Different configurations and layers of perovskite solar cells.*

1.3.5. Processes within a perovskite solar cell

On photoexcitation, generation of an exciton takes place within the perovskite. Depending on the energy absorbed by the perovskite and the binding energy of the excitons, they can separate and give rise to free charge carriers. Figure 1.8 depicts the various processes that can occur within a perovskite solar cell after absorption of light energy.

Process (i) in Figure 1.8 refers to the transfer of an electron from the conduction band of the perovskite to that of the ETL. Similarly, process (ii) refers to the transfer of holes from the valence band of the perovskite to that of the HTL. These two charge transfer processes majorly contribute to the output current obtained from solar cells. Hence, it is important to ensure that the ETLs and HTLs allow for an easy transfer of electrons and holes from the absorber layer to these layers. For this purpose, the electron transport material is chosen such that its conduction band lies just below that of the perovskite and the hole transport material is selected such that its valence band is just above that of the perovskite. Process (iii) refers to electron-hole recombination, which is radiative in nature. Pathways (iv)-(vii) are detrimental to the functioning and decrease the PCE of the solar cell. Processes (iv) and (v) correspond to the back transfer of electrons from the ETL to the perovskite and holes from the HTL to the perovskite respectively. Process (vi) results in the recombination of electrons and holes in the ETL and HTL. Process (vii) is a trap-assisted recombination pathway, which is non-radiative in nature. These processes are unfavourable for developing efficient solar cells and most efforts are driven towards extracting charge carriers into their respective layers and minimizing recombination pathways.[74]

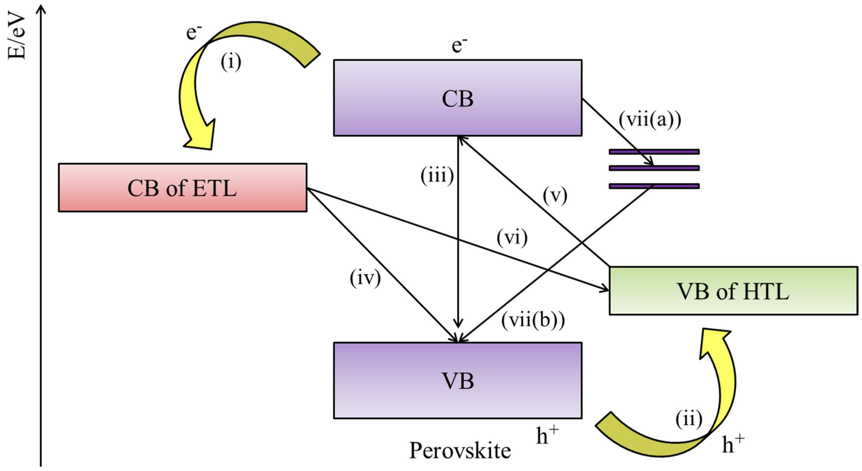

Figure 1.8. *Processes within a perovskite solar cell.*

1.3.5.1. Charge carrier recombination

Charge carrier recombination dynamics play a critical role in analysing the success of a semiconductor for solar cell applications. In metal halide perovskites, there are three major charge carrier recombination pathways.[75] First, is the non-radiative monomolecular process, known as the trap-assisted recombination (Figure 1.9(a)). This involves either an electron or a hole getting captured in a trap state and hence is monomolecular in nature. Studies on a variety of MHPs have revealed the presence of shallow trap states close to the band edge and very few deep trap states. The existence of traps is highly dependent on the material's processing conditions and mainly arises due to metal, halide or organic vacancies in the lattice.[75] The second recombination pathway is a bimolecular process corresponding to the intrinsic electron-hole recombination within the perovskite (Figure 1.9(b)). This recombination is radiative in nature and is responsible for the photoluminescence observed in perovskites. The final pathway is the Auger recombination, which is a many body process (Figure 1.9(c)).[76] In this process, an electron and hole recombine with the energy and momentum being transferred to another neighbouring electron or hole, thus resulting in non-radiative recombination. This process can involve a phonon absorption or emission as well. These pathways compete with the charge transfer process, are highly sensitive to charge carrier densities and in order to develop suitable devices, it is essential to understand the contribution of each of these processes to the recombination dynamics. In general, efforts are made to reduce non-radiative recombination which can be done by decreasing the trap states through a control on the processing conditions and by controlling the charge carrier densities based on the light source and temperature.[43,75,77]

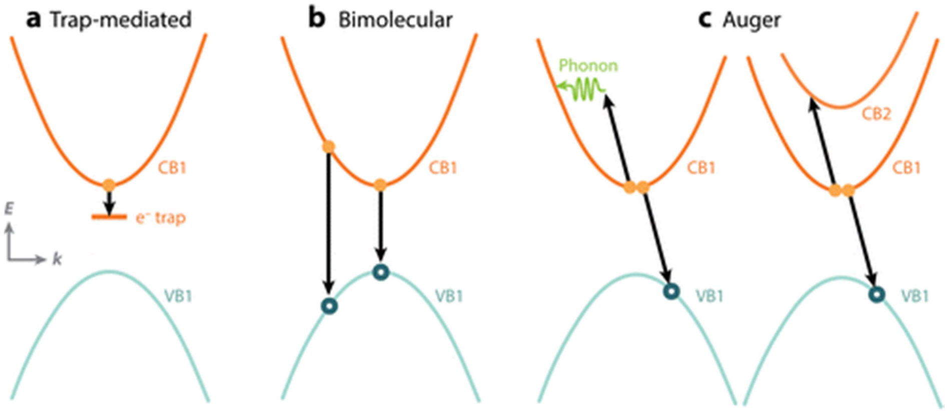

Figure 1.9. *Possible recombination pathways within perovskites after photoexcitation.*[75]

An understanding of the fundamental photophysics of metal halide perovskites is essential to achieve high performing solar cells. In addition to carrier generation and recombination dynamics, an analysis of the intrinsic carrier dynamics of the perovskite, particularly the carrier relaxation process, is crucial. High charge transfer rates, low recombination rates and slow carrier relaxation rates are some properties that define a good solar cell. These processes directly impact the rate at which light gets converted into electricity in these materials.

Chapter-2

Transient absorption spectroscopy and hot carrier relaxation process

2.1. Introduction

Transient absorption spectroscopy is a pump-probe spectroscopy technique which is used to study the time-dependent dynamics of a chemical system. It is a powerful tool for understanding photochemical and photophysical processes. This technique allows us to measure the changes in optical density as a function of wavelength and time. It makes use of two laser pulses – a pump and a probe. A sample is photo-excited using a pump pulse and the probe, generally white light, is then used to investigate the pump induced changes within the sample at various time delays. A mechanical delay line is used to vary the delay between the pump and the probe.

As this technique is used to study the changes brought in by the pump pulse, it is essential to eliminate the effect of the probe on the dynamics of the molecule. For this very purpose, the probe pulse is measured separately and then subtracted from the total absorption signal. This is done by using a chopper, which blocks every alternate pump pulse and the absorbance of the probe alone is recorded. The difference between the signals, when both the pump and probe are present and when only the probe is present, known as a differential absorption signal is then obtained.

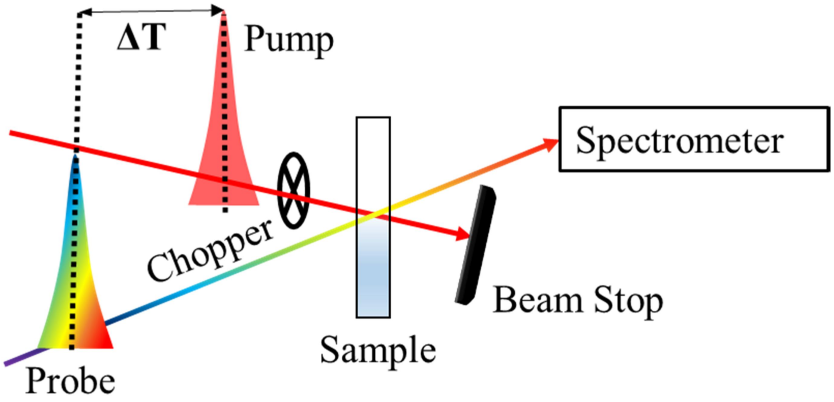

Figure 2.1. *Schematic of a pump-probe experiment.*

The differential absorption signal ($\mathbf{\Delta OD}$) is given as:

$$\mathbf{OD_{probe\,(pump\,on)}} = -\mathbf{log}\left(\mathbf{I_{probe\,(pump\,on)}}\right);\ \mathbf{OD_{probe\,(pump\,off)}} = -\mathbf{log}\left(\mathbf{I_{probe\,(pump\,off)}}\right)$$

$$\mathbf{\Delta OD} = \mathbf{OD_{probe\,(pump\,on)}} - \mathbf{OD_{probe\,(pump\,off)}}$$

$$= -\mathbf{log}\left(\mathbf{I_{probe\,(pump\,on)}}\right) + \mathbf{log}\left(\mathbf{I_{probe\,(pump\,off)}}\right)$$

$$\mathbf{\Delta OD = log\left(\frac{I_{probe\ (pump\ off)}}{I_{probe\ (pump\ on)}}\right)}$$

2.2. Transient absorption signals

There are three types of signals that can be obtained through transient absorption spectroscopy:

(i) **Ground state bleach (GSB)**: When the pump pulse excites a sample, some molecules from the ground state are transferred to an excited state. As a result, the probe pulse is absorbed by lesser number of molecules at the ground state wavelength. This results in a negative absorption signal being obtained, whose peak corresponds to that typically obtained by steady-state absorption. This signal is known as the ground state bleach.

(ii) **Stimulated emission (SE)**: When the probe pulse is incident on the sample, it can stimulate the emission of molecules from the excited state (created by the pump) to the ground state. This signal corresponds to stimulated emission. When the pump is on, the number of photons reaching the detector is a combination of the photons contained in the probe and the photons emitted from the molecules in the excited state of the sample. In contrast, when the pump is blocked, the number of photons reaching the detector are only those that are contained in the probe pulse. Hence, $I_{probe\ (pump\ on)} > I_{probe\ (pump\ off)}$. This results in a negative differential absorption signal for SE. Similar to spontaneous emission (fluorescence), stimulated emission also exhibits Stokes shift, in which the SE signal is red shifted as compared to the absorption signal. This shift is mainly due to the relaxation of the molecule and its immediate environment in the excited state.

(iii) **Excited state absorption (ESA) or Photo-induced absorption (PIA)**: Molecules in the excited state can absorb photons from the probe and get transferred to higher-lying excited states. This is known as excited state or photo-induced absorption. When the pump is on, molecules are excited from the ground to the excited state and further excitation to higher states takes place due to the probe. In the absence of the pump pulse, there is insufficient population in the excited state for absorption of the photons from the probe.

Thus, $\mathrm{OD}_{\mathrm{probe\ (pump\ on)}} > \mathrm{OD}_{\mathrm{probe\ (pump\ off)}}$ and a positive differential absorption signal is obtained corresponding to ESA.

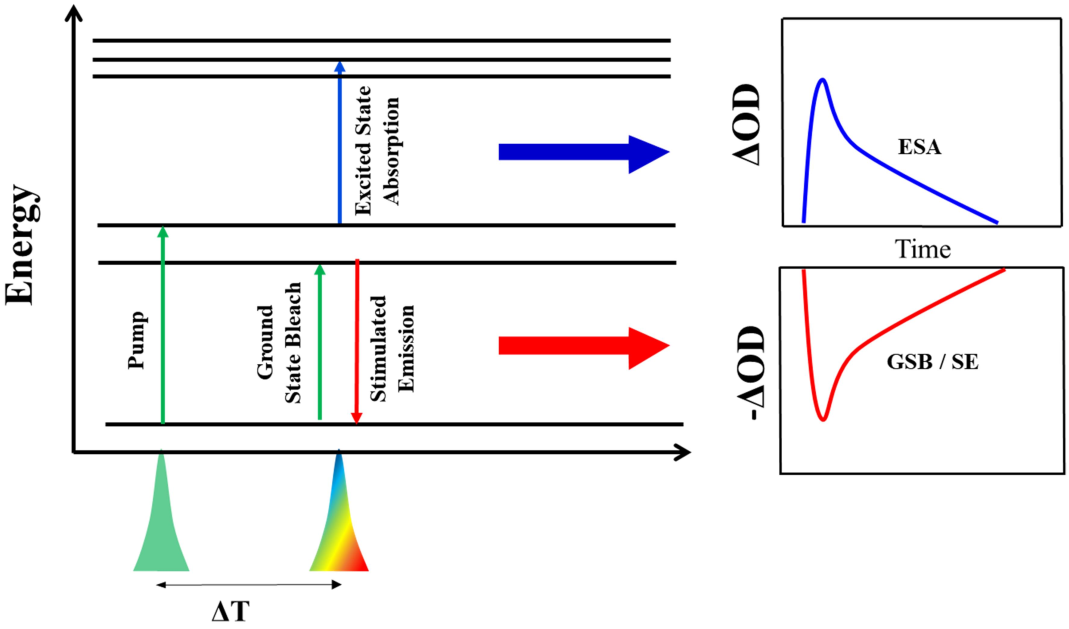

Figure 2.2. *Types of signals in a pump-probe experiment.*

2.3. Specifications of the instrument

A Ti-Sapphire amplified laser beam was used to generate a wavelength centred at 800 nm for our experiment. The repetition rate and pulse width of the laser was 1 kHz and 50 fs respectively. Using a beam sampler, the 800 nm laser beam was split into the pump and the probe. A BBO (β-barium borate) crystal was used to generate an excitation wavelength of 400 nm (pump pulse). The probe pulse was routed to a custom-made femtosecond transient absorption spectrometer (TAS, Newport Inc. USA) and was vertically polarised. The pump was set at a magic angle of 54.7˚ using a half wave plate in both the arms. A CaF_2 crystal was used to generate a broad continuum of light in the visible and near-IR region and was placed on a motorised translation stage. A variable neutral density filter was used at the sample position to control the intensity of the probe pulse. Every alternate pump pulse was blocked using a mechanical chopper (New Focus 3502, with a 7/5 slot wheel, Newport Corp), which was placed in the pump arm operating at a 500 Hz repetition rate. The probe was spectrally overlapped with the pump beam, collimated and sent into the spectrograph (Oriel MS260i, Newport Corp). A spectrometer with 1200 grooves/mm grating (Richardson grating 74064, Newport Corp) was used to detect the transmitted probe pulse with the help of a linear array detector (CMOS S10453-1024Q, Hamamatsu Photonics). A software-controlled mechanical delay line (ILS300LM, Newport Corp) was used to vary the time delay between the pump and probe pulse.

2.4. Excited state dynamics of perovskites using transient absorption spectroscopy

Transient absorption spectroscopy can be used to study the dynamics of perovskites in the form of a solution or thin film, to analyse its use for photovoltaic and other optoelectronic applications. In case of solutions, perovskite microcrystals or nanocrystals can be used to understand the intrinsic dynamics and rates of various processes, such as carrier relaxation, electron-hole recombination, trap-assisted recombination etc., within this material. For thin films (comprising of ETL and HTL), this technique provides us with essential information regarding electron and hole transfer rates (Figure 2.3).

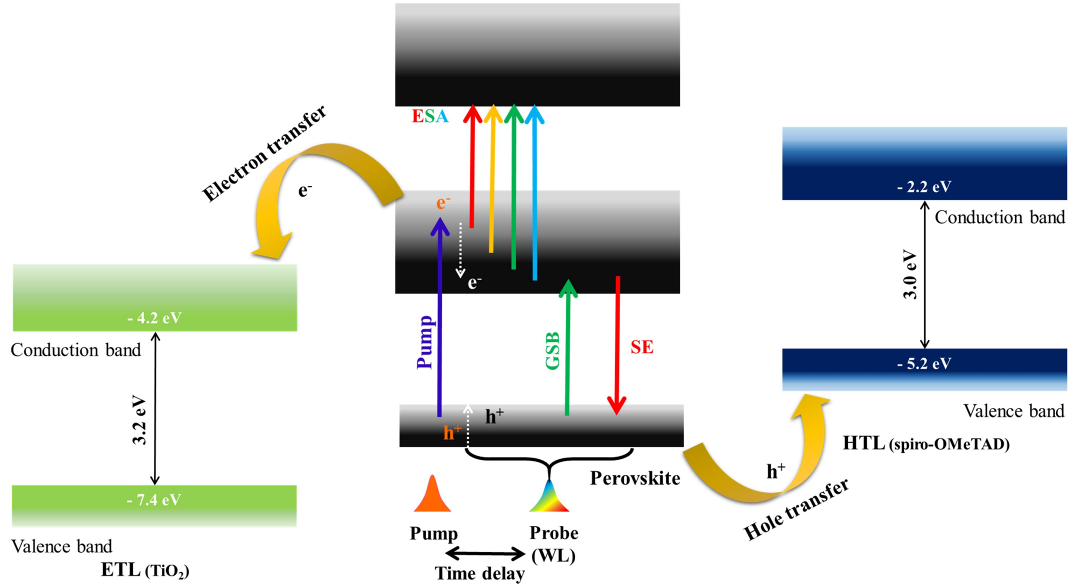

Figure 2.3. *Different processes and signals obtained using TA spectroscopy in perovskites.*

2.4.1. Hot carrier relaxation in perovskites

When light is absorbed by a solar cell, photons containing energy higher than the bandgap of the semiconductor result in the generation of excitons or free charge carriers with excess energy. These charge carriers or excitons, which possess a temperature higher than the lattice temperature are referred to as “hot” carriers or “hot” excitons. In case of most semiconductors, these hot species readily lose their excess energy to phonons or in the form of heat.[78]

Materials that have slow hot carrier relaxation rates can be used for the development of hot carrier solar cells (HCSCs). HCSCs are based on the concept of the extraction of electrons and holes into the outer circuit while they are hot, resulting in increased voltages in solar cells.[79] They have the potential to overcome the conventional single junction SQ limit of 33% and instead can have a maximum efficiency of 67%, if all the hot species are extracted into their respective charge extraction layers before cooling.[80] In this direction, perovskites have shown to possess slow hot carrier relaxation rates, thereby opening doors to the manufacturing of HCSCs using perovskites as the absorber layer.

On absorption of high energy photons, the hot carriers initially redistribute their energy in accordance with Fermi-Dirac statistics and attain a carrier temperature T_C, which is higher than the lattice temperature T_L. This process is known as thermalisation. Eventually, these thermalized carriers lose their energy through inelastic carrier-phonon interactions, resulting in the hot carriers relaxing to the band edge with a loss of their excess energy. This process is known as hot carrier cooling.[80]

In 2013, Sum et. al. reported the first study on hot carrier cooling in $MAPbI_3$ polycrystalline films using TA spectroscopy. A hot carrier cooling time of 0.4 ps was obtained at a pump energy of 3.1 eV and this was attributed to the hot-hole relaxation process.[81] This rate is slower as compared to organic semiconductors (~100 fs) and matches well with the relaxation times obtained in case of inorganic semiconductors such as GaAs. Subsequently, a lifetime of 0.4 ps was obtained in these films corresponding to the hot-electron relaxation process as well.[82] These preliminary results demonstrated great potential in perovskites to be developed as HCSCs. The hot carrier relaxation process has been shown to be pump-fluence dependent, with an even slower hot carrier cooling time of about 10 ps being obtained in $MAPbI_{3-x}Cl_x$ films at a pump fluence of 340 $\mu J/cm^2$.[83]

These hot carrier cooling rates are dependent on the initial excess energy of the hot carrier, photoexcited carrier density,[84] cation species, morphology and resolution of the instrument used for measurement.[85]

2.4.1.1. Reasons for slow hot carrier relaxation in perovskites

Hot carrier relaxation majorly occurs within 1 ps via the electron-longitudinal optical (LO)-phonon scattering process. Optical phonons (lattice vibrations) refer to out-of-phase movements in which a dynamic dipole moment is introduced within the crystal system through the electric field of light. These can be present in the transverse or longitudinal modes. This scattering is also referred to as the Fröhlich process and hot carrier relaxation occurs with the emission of LO phonons till the band edge is reached.[86] The exact mechanism of this cooling process is not yet completely understood, but several processes such as phonon bottleneck effect, polaron formation, Auger heating etc. are responsible for the slow cooling rates observed in perovskites.[78]

As carrier cooling mainly depends on the emission of LO phonons, a high density of these phonons can be produced in certain cases, resulting in the formation of a "phonon bottleneck". This results in some amount of the phonon energy scattering back, which then re-heats the carriers, thus slowing down the cooling process.[87] At high pump fluence, this phonon bottleneck effect has been observed in $MAPbI_3$ and $FAPbI_3$ films with decreased cooling rates.[84,88] At high hot carrier densities ($\sim 10^{19}$ cm^{-3}), Auger heating predominates and reduces hot carrier relaxation rates due to transfer of the recombination energy to another charge carrier.[89] Other effects such as large polaron formation at low carrier densities[90] and band-filling[91] at high carrier densities further slow down hot carrier cooling in perovskites.

Using a sequence of ultrafast optical pulses (pump-push-probe spectroscopy), the hot carrier cooling times for $FAPbI_3$, $FAPbBr_3$, $MAPbI_3$, $MAPbBr_3$, and $CsPbBr_3$ have been obtained in the range of 100-900 fs, in accordance with lifetimes determined through other methods as well.[92] This cooling time increased with an increase in the carrier density. Bromide based perovskites tend to have a higher cooling time as a result of their stronger electron-phonon coupling.[92] Ultrafast PL measurements on $MAPbI_3$ thin films have shown fast rates of hot-hole relaxation dependent on the closeness of the excitation to the band edge. Rise times of the order of 100-300 fs were obtained when the excitation was well above the bandgap and much longer rise times of 300-700 fs were obtained as the excitation reached closer to the bandgap. A much slower timescale of 1-10 ps was observed for hot-electron relaxation.[93] A long lived PL of 150 ps in $MAPbBr_3$ and $FAPbBr_3$ single crystals and about a few nanoseconds in case of $FASnI_3$ thin films have been attributed to the slow hot carrier relaxation process.[91] TA spectroscopy on the nanocrystals of the double perovskite $Cs_2AgBiBr_6$ has revealed a hot electron relaxation time of 0.8 ps (from the fast PIA band decay) and a hot hole relaxation time of 0.2 ps (from the fast GSB buildup signal).[94]

Given the slow hot carrier relaxation rates in metal halide perovskites, several studies on the transport and extraction of these hot carriers have yielded promising results for developing HCSCs. Long range hot carrier transport has been reported for $MAPbI_3$ films using ultrafast transient absorption microscopy.[95] Efficient hot carrier extraction is one of the most important components for manufacturing suitable HCSCs since these hot carrier relaxation rates compete with the charge transfer process. TA spectroscopy has been used to deduce hot carrier extraction through the disappearance of the hot-energy tail in case of $CsPbI_3$ films with P3HT as the HTL.[96] Ultrafast hot carrier transfer (~300 fs) has been reported for $CsPbBr_3$ nanocrystals using benzoquinine and phenothiazine as the ETL and HTL respectively.[97] To truly realise the use of perovskites in HCSCs further research is required in areas such as identifying the suitable energy contacts and the optimal layer thickness for harvesting these hot carriers.[98] Additionally, as double perovskites overcome the challenges faced by $MAPbI_3$ and other organic-inorganic and all-inorganic perovskites, it is essential to study the hot carrier relaxation process in these materials, to exploit their properties for the development of HCSCs.

Chapter-3

Excited state dynamics of $Cs_4CuSb_2Cl_{12}$ double perovskite

3.1. Introduction

$Cs_4CuSb_2Cl_{12}$ (CCSC) is a double perovskite of the form $A_4B^{II}B_2^{III}X_{12}$, in which four Pb^{2+} cations are replaced by one Cu^{2+} and two Sb^{3+} ions. A layer of $[CuCl_6]^{4-}$ octahedra is sandwiched between two $[SbCl_6]^{3-}$ octahedra with corner sharing chloride ions. The Cs^+ cation is present in the vacant sites between these octahedral layers. This perovskite allows for the use of benign, earth-abundant elements to replace lead, thus helping overcome the toxicity issues raised by lead halide perovskites. The first paper to report the synthesis of CCSC was by Solis-Ibarra et. al. in 2017.[99] They prepared microcrystals of this perovskite using the acid-precipitation method. Single crystal studies of CCSC revealed a monoclinic *C*2/*m* crystal structure (Figure 3.1(a)). A triple-layered perovskite was obtained instead of a 3D structure, which was attributed to the vacancy created by antimony owing to its 3+ charge. Since CCSC consists of Cu in the 2+ state, it has a d^9 configuration. This results in Jahn-Teller distortion, with the axial bond lengths 0.52 Å longer than the other four bonds (Figure 3.1(b)). The as-synthesised perovskite had a direct bandgap of 1.0 eV, conductivity value one magnitude higher as compared to $MAPbI_3$ and high carrier mobility. It displayed photo and thermal stability, with no decomposition in the presence of humidity for upto 100 days.[99] These properties reveal tremendous potential for CCSC to be used for photovoltaic applications.

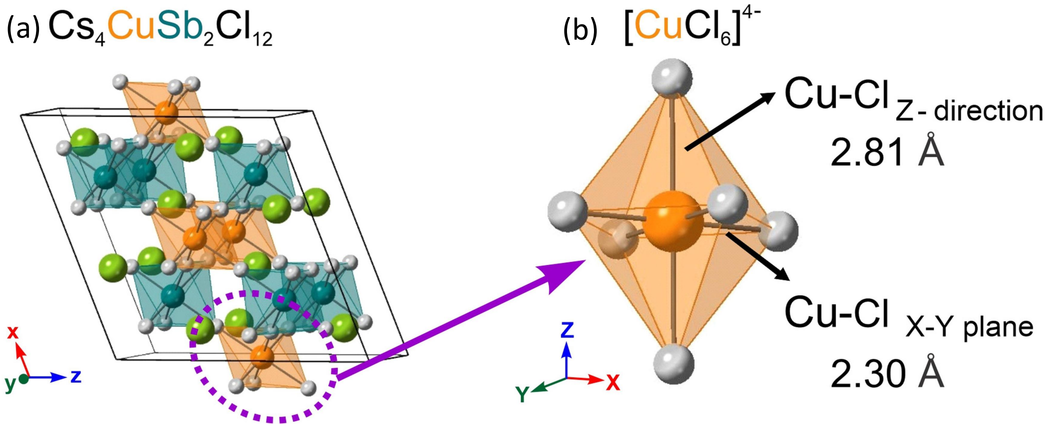

Figure 3.1. *(a) Monoclinic C2/m structure of CCSC (b) Jahn-Teller distortion in* $[CuCl_6]^{4-}$ *octahedra of CCSC.*[100]

Efforts have been made to synthesise the microcrystals (MCs) and nanocrystals (NCs) of CCSC through different synthesis methods. MCs of CCSC have been prepared via the mechanochemical synthesis[101] and liquid-phase synthesis methods[101,102], whereas the nanocrystals have been synthesised through the colloidal[100] and ultrasonic exfoliation method.[103] The experimental bandgap of the as-synthesised microcrystals range from 0.97-1.16 eV, with a direct bandgap[102] nature being observed in some cases and indirect in some other.[101] This suggests that the direct and indirect bandgap values are close to each other in CCSC, due to low band dispersion resulting in a nearly flat conduction band,.[101,104] Density-functional theory (DFT) calculations in case of MCs reveal a similar bandgap as experimentally determined (Table 3.1).[99,101] CCSC nanocrystals on the other hand have been reported to have a direct bandgap, with values lying in the range of 1.60-1.79 eV.[100,103] Computationally obtained values don't seem to be in good agreement with the experimental results in case of NCs (Table 3.1).[100,103] A general trend that can be observed as we go from microcrystals to nanocrystals is the increase in the bandgap values. This can be attributed to the quantum confinement effect,[100] where semiconductors in the nanoregime tend to have higher bandgaps as compared to their bulk counterparts due to less overlap between the energy levels (more discrete energy levels). Surface coating ligands or atomic arrangements can also result in such differences in bandgaps.[100] Table 3.1 summarises the synthesis methods and bandgaps obtained in different studies.

Method of Synthesis	**Nano/ microcrystals**	**Computational band gap (eV)**	**Experimental band gap (eV) (considering direct)**	**Experimental band gap (eV) (considering indirect)**
Acid precipitation[99]	Micro	0.98	-	1.00
Mechanochemical[101]	Micro	1.10	1.14	0.97
Liquid phase[102]	Micro	-	1.16	-
Colloidal[100]	Nano	1.24	1.79	-
Ultrasonic exfoliation[103]	Nano	0.91	1.60	-

Table 3.1. *Different reported synthesis methods of CCSC and the corresponding experimental and theoretical bandgaps*

MCs of CCSC have not shown any photoluminescence (PL), despite multiple attempts.[101] While PL wasn't observed in CCSC NCs prepared via the colloidal synthesis route,[100] a weak and broad PL signal at 632 nm was observed in case of the nanocrystals synthesised through the ultrasonic exfoliation technique.[103] The weak or non-detectable PL signal in case of both MCs and NCs has been attributed to an ultrafast carrier trapping process due to exciton-phonon coupling[100] as well as the presence of surface trap states,[101,103] which strongly competes with the radiative recombination process responsible for PL. This raises concerns regarding the defect tolerance of CCSC, which requires further investigation.

The study by Solis-Ibarra et. al. reported a computationally-obtained direct bandgap of 0.98 eV for CCSC.[99] This DFT calculation was performed using the semi-local Perdew, Burke, and Ernzerhof (PBE) functional,[105] which treats spin states as degenerate. The Fermi level lies in the valence bands, which incorrectly indicates a metallic behaviour in contrast to the semiconducting nature of the material.[99] This inconsistency was obtained since the spin states aren't degenerate in case of CCSC due to the presence of an unpaired electron in Cu^{2+}. Spin-polarised DFT studies have been performed, using different functionals (PBE, PBE+U and HSE) and assuming different magnetic ordering within this material.[104] These results suggest that CCSC is the most stable in the antiferromagnetic state, has a less dispersive band structure and an indirect bandgap of 1.0 eV. PBE+U functional provides the best representation of this system, which is well in accordance with the experimentally obtained values. HSE overestimates the bandgap by about 0.7 eV and is a better fit for Cu^{+} containing compounds. The density of states (DOS) calculations reveal that the valence band contributions are mainly from Cl 3p and Sb 4s, with a minor contribution from Cu 3d as well. On the other hand, the conduction band minimum comprises of Cu 3d and Cl 3p majorly. Thus, to get a reasonable band structure of CCSC, it is important to take into account the magnetic ordering of the compound, strong correlation of the d states in Cu^{2+} and the lifting of the spin degeneracy.[104]

CCSC has shown to be phase-stable upto 200 ^{o}C in an ambient environment. A black-to-yellow-to-black transformation has been observed as CCSC is first heated beyond 200 ^{o}C and then cooled to room temperature in a humid environment. CCSC decomposes into $Cs_3Sb_2Cl_9$, Cs_2CuCl_4 and $SbCl_3$ on heating and returns back to the perovskite state with some impurities when cooled.[101] This material is stable under ambient conditions for several months and in polar solvents containing < 30% water. EPR studies reveal the presence of an unpaired electron, corresponding to the d^9 configuration of Cu^{2+} cation and other magnetic studies indicate a long range magnetic ordering from 2-400 K in this material.[101] CCSC NCs synthesised using a top-down approach through ultrasonic exfoliation of the MCs have a bandgap of 1.6 eV and a more dispersive band structure. The absorption spectra and Ultraviolet photoelectron spectroscopy (UPS) studies of the NCs revealed the valence band maximum (VBM), conduction band minimum (CBM) and Fermi level as -3.74, -5.34, -4.56 eV respectively. The as-synthesised CCSC NCs exhibit a p-type semiconductor behaviour. Time-resolved transient absorption spectroscopic studies on these NCs resulted in three time components being obtained, corresponding to 14 ps, 697 ps and >5 ns. These time components were assigned to the charge trapping, radiative recombination and trap-assisted recombination processes respectively. This reveals the presence of abundant trap states, resulting in the charge trapping process strongly competing with the radiative recombination process.[103]

Overall, CCSC offers facile synthesis methods, is stable to heat, light and humidity and has a suitable bandgap for optoelectronic applications. CCSC MCs and NCs have shown promise as photodetectors and solar absorbers,[99–103] and with further research properties of this material can be improved for several applications. Till date, no studies have been carried out on determining the position of the valence band and conduction band in case of CCSC microcrystals. Recently, perovskites have shown slow hot carrier relaxation rates which is useful for the development of hot carrier solar cells. Here in, using techniques such as XPS and UPS, we hope to understand the band structure and the band levels of this material better. Additionally, using femtosecond transient absorption spectroscopy, we aim to understand the excited state dynamics, in particular, the hot carrier relaxation process of the as-synthesised microcrystals.

3.2. Experimental Techniques

3.2.1. Steady-state absorption

All absorption spectra were recorded using an Agilent Technologies Cary 5000 UV-Vis-Near-IR Spectrophotometer in the range of 400 nm to 800 nm. A quartz cuvette of 1 cm path length was used for the measurement. As the solubility of CCSC was tested in different solvents (toluene, chlorobenzene, 1,2-dichlorobenzene), each of these solvents was used as a baseline for each individual spectrum.

3.2.1.1. Tauc plot from UV-Vis spectroscopy

A Tauc plot was used to determine the direct and indirect bandgap of the as-prepared CCSC microcrystals from its absorption spectrum. A plot of $(\alpha h\nu)^2$ vs hν (photon energy) according to equation (3.1) was constructed, whose x-intercept corresponded to the direct bandgap value. Similarly, a plot of $(\alpha h\nu)^{1/2}$ vs hν (equation 3.2) was made to determine the indirect bandgap.

$$(\alpha h\nu)^2 = k\,(h\nu - E_g) \qquad \ldots \text{ equation (3.1)}$$

$$(\alpha h\nu)^{1/2} = k\,(h\nu - E_g) \qquad \ldots \text{ equation (3.2)}$$

Here, $\alpha = \frac{1}{t} 2.303 \log A$ = absorption coefficient, k = constant, E_g = bandgap, A = absorbance and t = thickness of cuvette.

3.2.2. Infrared (IR) Spectroscopy

The IR spectrum was recorded in the transmittance mode using a Bruker IFS 66/S spectrometer. The spectrum was obtained at a spectral resolution of 4 cm^{-1} and 2.2 KHz as the scanning velocity in the 4000–500 cm^{-1} range, under ambient conditions.

3.2.3. Raman Spectroscopy

The Raman spectrum was measured using a Renishaw Raman spectrometer with a 785 nm laser source. The spectrum was recorded in the 4000-50 cm^{-1} range, using high-resolution gratings of 1200 lines/mm for a scan time of 10 s.

3.2.4. Powder X-ray diffraction (PXRD)

PXRD data were recorded on a Rigaku Ultima IV diffractometer using Cu Kα (λ = 1.54 Å) radiation. CCSC powder was deposited on the glass substrates to obtain the XRD patterns. The data was collected within the 2θ range of 10–50° with a scanning speed of 5° per min.

3.2.5. Scanning Electron Microscopy (SEM)

To characterize the morphology of CCSC, a JEOL JSM-7600F Scanning Electron Microscope was used. The sample was drop casted on a silicon wafer and the solvent was allowed to vaporise under ambient conditions.

3.2.5.1. Energy-dispersive X-ray spectroscopic analysis (EDAX)

EDAX measurements were carried out to confirm the presence of Cs, Cu, Sb and Cl elements.

3.2.6. Dynamic Light Scattering (DLS)

Size distribution measurement of CCSC was carried out by dynamic light scattering, using Zetasizer, Nanoseries, Malvern Instruments DLS spectrometer.

3.2.7. X-Ray Photoelectron Spectroscopy (XPS)

XPS spectra were recorded on a ThermoFisher Scientific Nexsa X-Ray Photoelectron Spectrometer using Al Kα = 1486.6 eV radiation.

3.2.8. Ultraviolet Photoelectron Spectroscopy (UPS)

UPS spectra were recorded on a ThermoFisher Scientific Nexsa XPS instrument using ionisation radiation of 21.2 eV (He I).

3.2.9. Femtosecond transient absorption spectroscopy

Details of the technique are discussed in Chapter 2.

3.3. Synthesis of CCSC microcrystals

3.3.1. Materials required

Cesium chloride (99.9%), copper chloride (99%; anhydrous) and antimony chloride (99.95%) were purchased from Sigma-Aldrich. Methanol (spectroscopic grade) was purchased from Merck; toluene (99.5%), chlorobenzene (99.9%), 1,2- dichlorobenzene (99%), isopropanol (99.5%), chloroform (99%), oleic acid (99%) and hydrochloric acid were purchased from Sigma-Aldrich and used as solvents without any further purification.

3.3.2. Preparation of CCSC microcrystals

The synthesis of CCSC was carried out according to a reported protocol[101] with slight modifications. 0.5 mmol of $SbCl_3$ and 0.25 mmol of $CuCl_2$ were dissolved in 10 ml of methanol. In a separate beaker, 0.6 mmol of CsCl was dissolved in 100 μL of water. The

CsCl solution was added dropwise to the first solution, resulting in the immediate precipitation of a black compound. The mixture was sonicated for 30 s and then centrifuged at 5000 rpm for 4 mins. The supernatant was separated and the powder settled at the bottom was collected. The as-synthesised CCSC MCs were allowed to dry under vacuum in a desiccator for a day. They were then stored in a vial under ambient conditions for further use.

3.3.3. Solubility in different solvents

The as-synthesised CCSC MCs were insoluble in $CHCl_3$, which was not in agreement with earlier studies.[103] Therefore, a solubility test was conducted to determine which solvent would be the best for forming a stable colloidal solution. Several solvents such as toluene, chlorobenzene, 1,2-dichlorobenzene, isopropanol and $CHCl_3$ + oleic acid in HCl were used. 3 mg of CCSC was dissolved in 6 ml of every solvent. The results obtained are displayed in Figure 3.2. Within 2 hours, CCSC settled down in case of $CHCl_3$ + oleic acid and 1,2-dicholorobenzene. In isopropanol, CCSC degraded immediately, resulting in a yellow residue. After about 12 hours, considerable amounts of CCSC remained dissolved in chlorobenzene and toluene, and thus these solvents were used for further characterization.

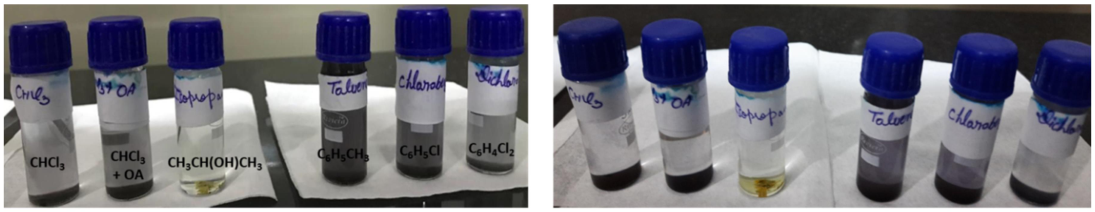

Just after sonication

After 2 hrs

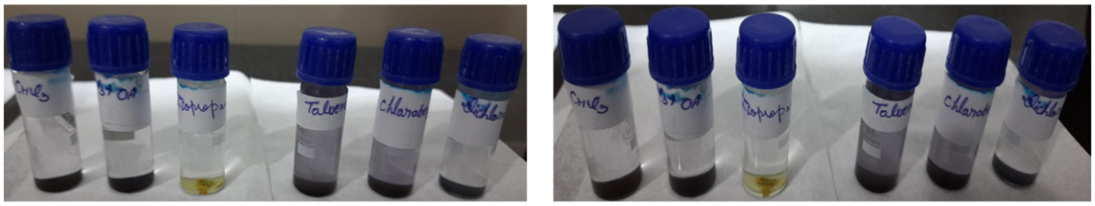

After 4 hrs

After 12 hrs

__Figure 3.2.__ Solubility of CCSC in different solvents.

3.4. Results and Discussion

3.4.1. Steady-state absorption

The as-synthesised CCSC MCs show absorbance in the range of 500-1000 nm. An absorbance peak is obtained at 590 nm, as shown in Figure 3.3. The existence of the absorption tail in the spectrum points to the presence of sub-bandgap states in CCSC. While CCSC dissolved in chlorobenzene and toluene have nearly the same absorbance peak, the intensity of absorbance in toluene is considerably lower and a much broader peak is obtained.

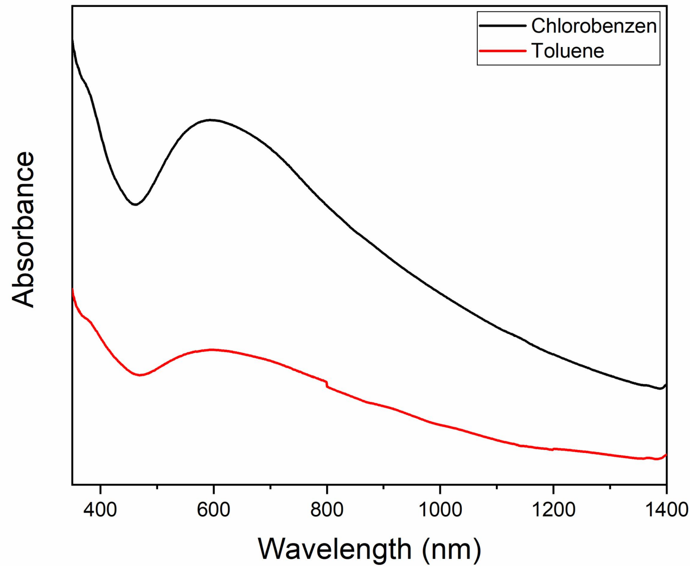

Figure 3.3. *Steady state absorption spectra of CCSC MCs in chlorobenzene and toluene.*

3.4.1.2. Tauc plot from UV-Vis spectroscopy

The tauc plot of the as-synthesised CCSC MCs exhibits a direct bandgap of 1.87 eV (Figure 3.4 (a)) and an indirect bandgap of 1.66 eV (Figure 3.4 (b)). Hence, the lowest energy bandgap is indirect in nature in CCSC. However, the direct and indirect bands are very close to each other energetically, which could be a result of low band dispersion.

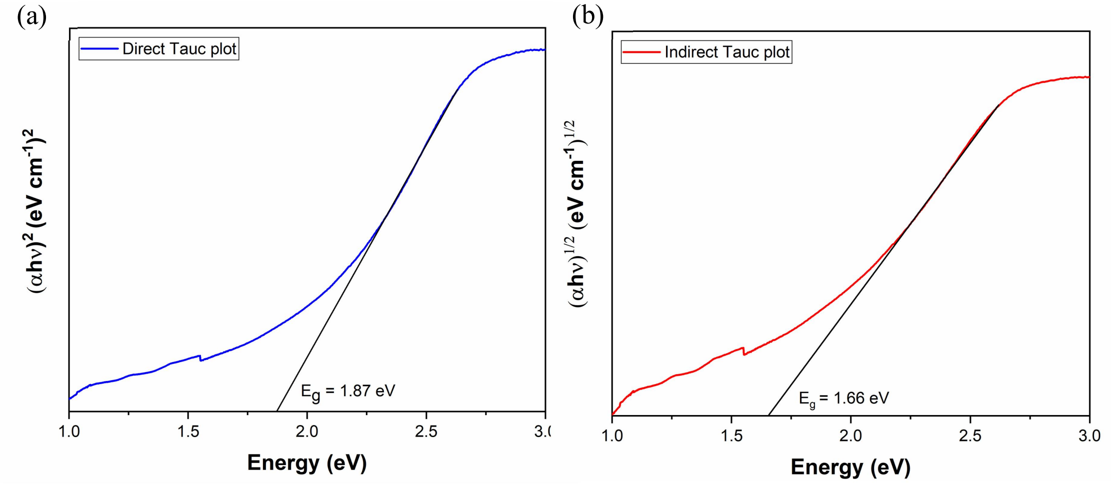

Figure 3.4. *Tauc plot of CCSC MCs considering (a) direct bandgap nature and (b) indirect bandgap nature.*

3.4.2. Infrared (IR) Spectroscopy

The FT-IR spectrum shows a strong peak at 617.50 cm^{-1} corresponding to the metal-halide stretching frequency, as displayed in Figure 3.5. The other peaks, namely 3395.25, 1637.25, 1402.30 and 1115.25 cm^{-1} correspond to the O-H, C-H and C-O stretching frequencies. We attribute this to the presence of traces of methanol, which was used as a solvent during sample preparation.

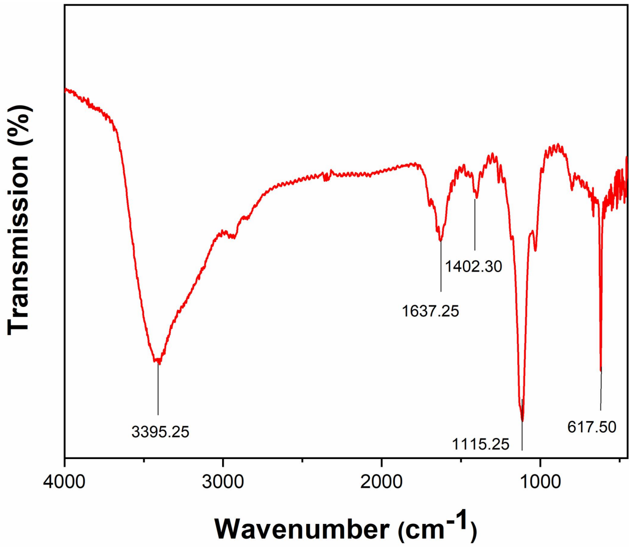

Figure 3.5. *IR spectrum of CCSC MCs.*

3.4.3. Raman Spectroscopy

The Raman spectrum shows peaks at 560, 280 and 156 cm^{-1}, which corresponds to different metal-halide stretching and bending frequencies in CCSC.

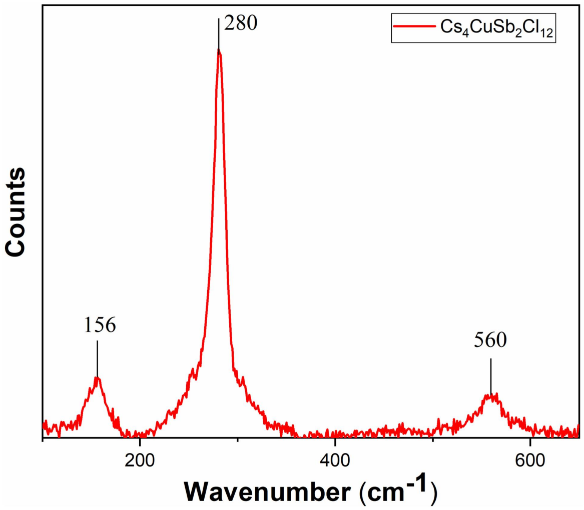

Figure 3.6. *Raman spectrum of CCSC MCs.*

3.4.4. Powder X-ray diffraction (PXRD)

Figure 3.7 shows the PXRD pattern of CCSC, which confirms that the black powder prepared by the solution-phase method rightly corresponds to the previously reported monoclinic *C*2/*m* crystal structure of CCSC.[99] The as-synthesised crystals are phase-pure and do not reveal the presence of the precursor salts. The Miller indices of the crystal planes corresponding to the peaks obtained in the PXRD pattern are shown in Figure 3.7.

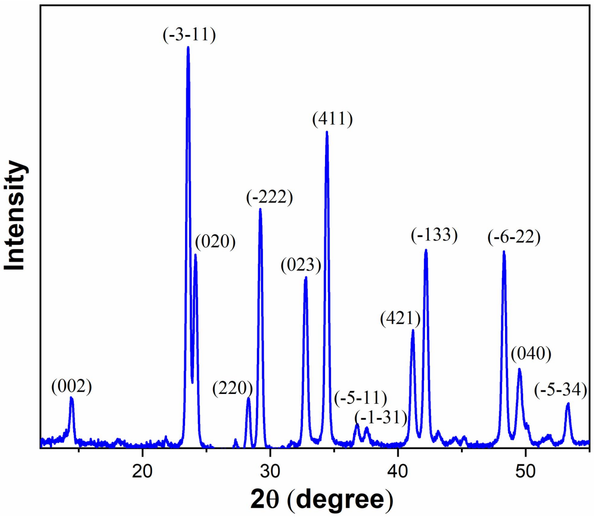

Figure 3.7. *PXRD pattern of as-synthesised CCSC MCs.*

3.4.5. Scanning Electron Microscopy (SEM)

The surface morphology and structure of the as-synthesised CCSC MCs were obtained using SEM. The image (Figure 3.8) reveals that the MCs are irregular in shape, crystalline in nature and have a variable size of a few micrometers.

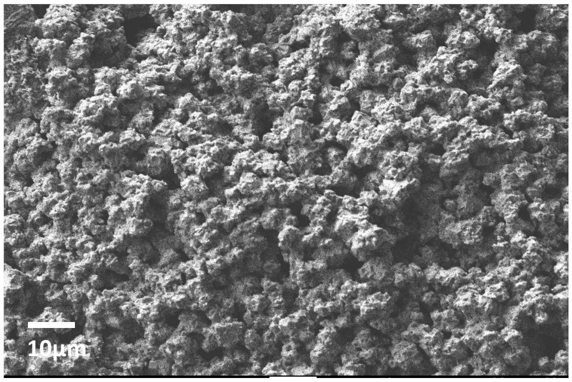

Figure 3.8. *SEM image of the as-synthesised CCSC MCs.*

3.4.5.1. SEM Energy-dispersive X-ray spectroscopic analysis (EDAX)

Figure 3.9 shows the EDAX elemental mapping images of the as-synthesised CCSC MCs. The homogenous density of dots suggests that each of the elements, Cs, Cu, Sb and Cl are uniformly distributed, resulting in a homogenous stoichiometry of CCSC throughout the sample.

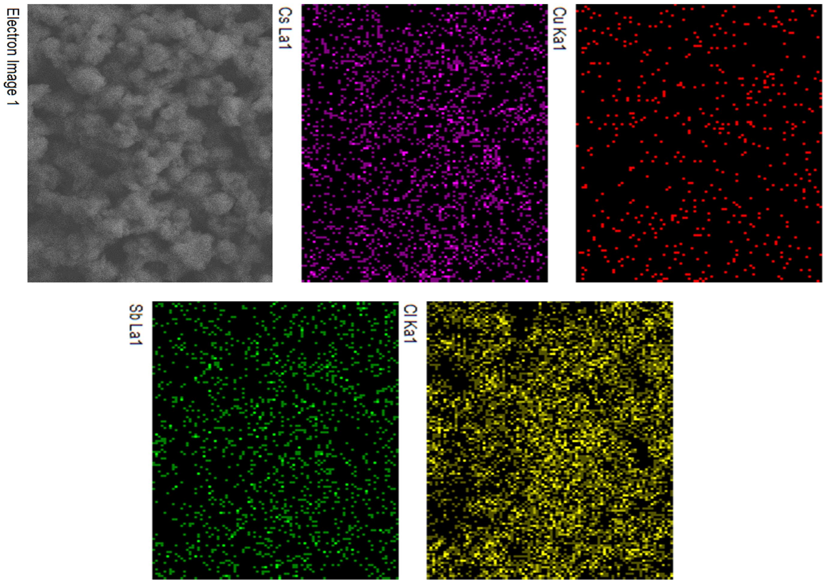

Figure 3.9. *Elemental mapping images of CCSC MCs.*

EDAX analysis confirms the presence of Cs, Cu, Sb and Cl elements in the sample. It also provides the atomic and weight % of each element as shown in Figure 3.10. The closeness of the chemical formula obtained from the elemental analysis to the expected formula reflects the purity of the sample and the success of the solution phase synthesis method.

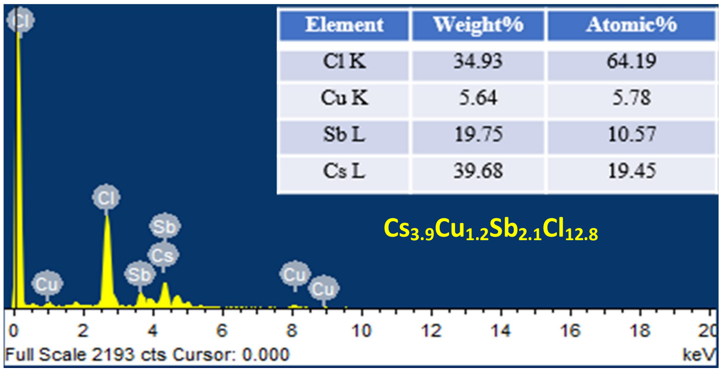

Element	Weight%	Atomic%
Cl K	34.93	64.19
Cu K	5.64	5.78
Sb L	19.75	10.57
Cs L	39.68	19.45

$Cs_{3.9}Cu_{1.2}Sb_{2.1}Cl_{12.8}$

Figure 3.10. *EDAX analysis of CCSC MCs.*

3.4.6. Dynamic Light Scattering (DLS)

The size distribution of CCSC MCs as measured using DLS is shown in Figure 3.11. The maximum distribution is obtained around 0.9 μm (900 nm).

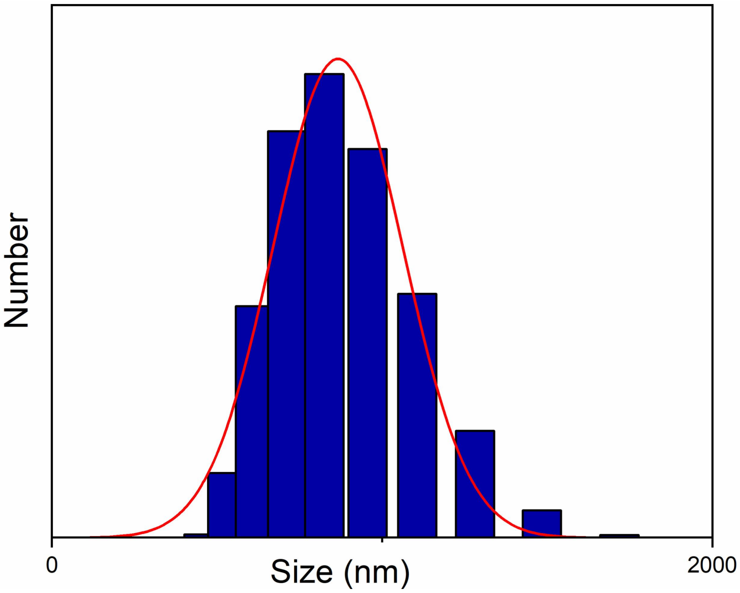

Figure 3.11. *Size distribution of CCSC MCs as measured through DLS.*

3.4.7. X-ray Photoelectron Spectroscopy (XPS)

The XPS spectra of the as-synthesised CCSC MCs further confirmed the presence of Cs, Cu, Sb and Cl ions. The HR-XPS spectra of each of the elements, with information about the orbitals in which the core electrons are present are shown in Figure 3.12.

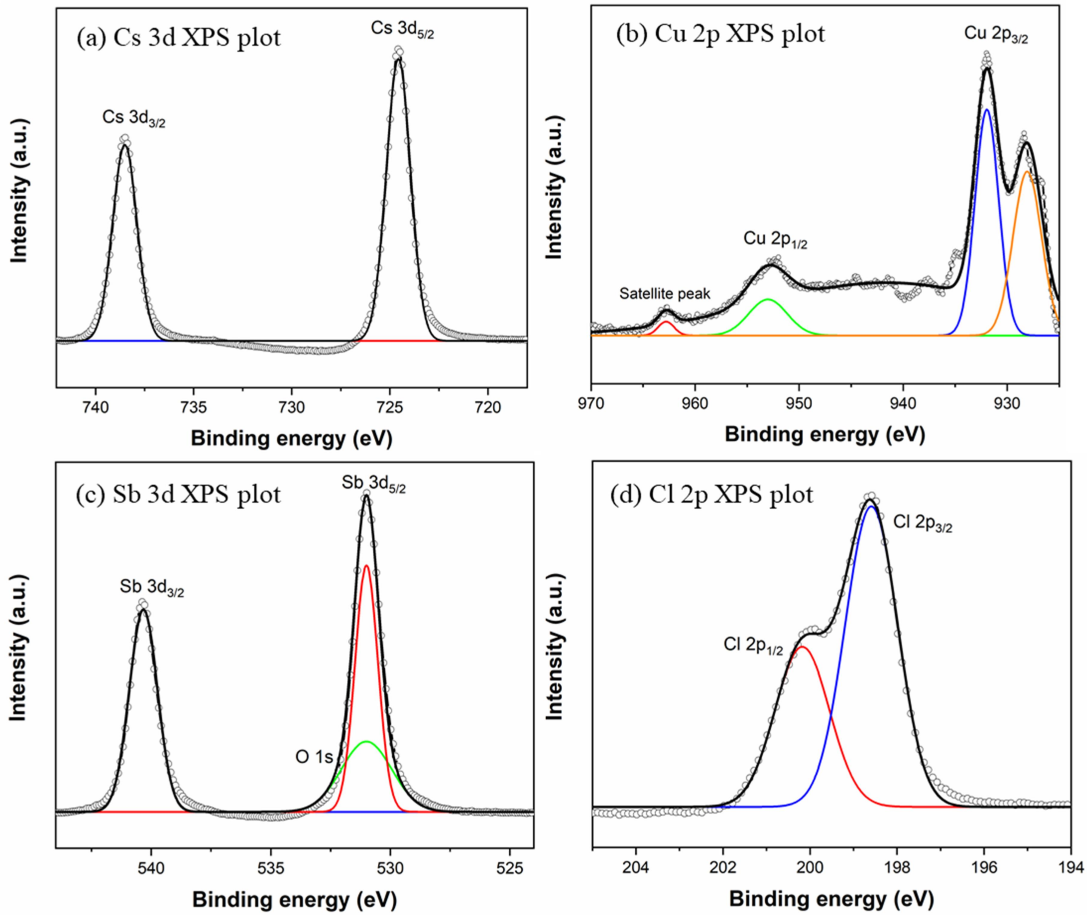

Figure 3.12. *XPS spectra for (a) Cs 3d, (b) Cu 2p, (c) Sb 3d and (d) Cl 2p of CCSC MCs.*

3.4.8. Ultraviolet Photoelectron Spectroscopy (UPS)

The UPS survey spectrum of CCSC MCs is shown in Figure 3.13 (a). Through this measurement and using equations (3.3) and (3.4), the work function and the valence band maxima of the material was obtained as 5.05 eV and 6.64 eV respectively.

$$\Phi = h\nu - (E_{cutoff} - E_F) \qquad \text{… equation (3.3)}$$

$$VBM = \Phi + E_{onset} \qquad \text{… equation (3.4)}$$

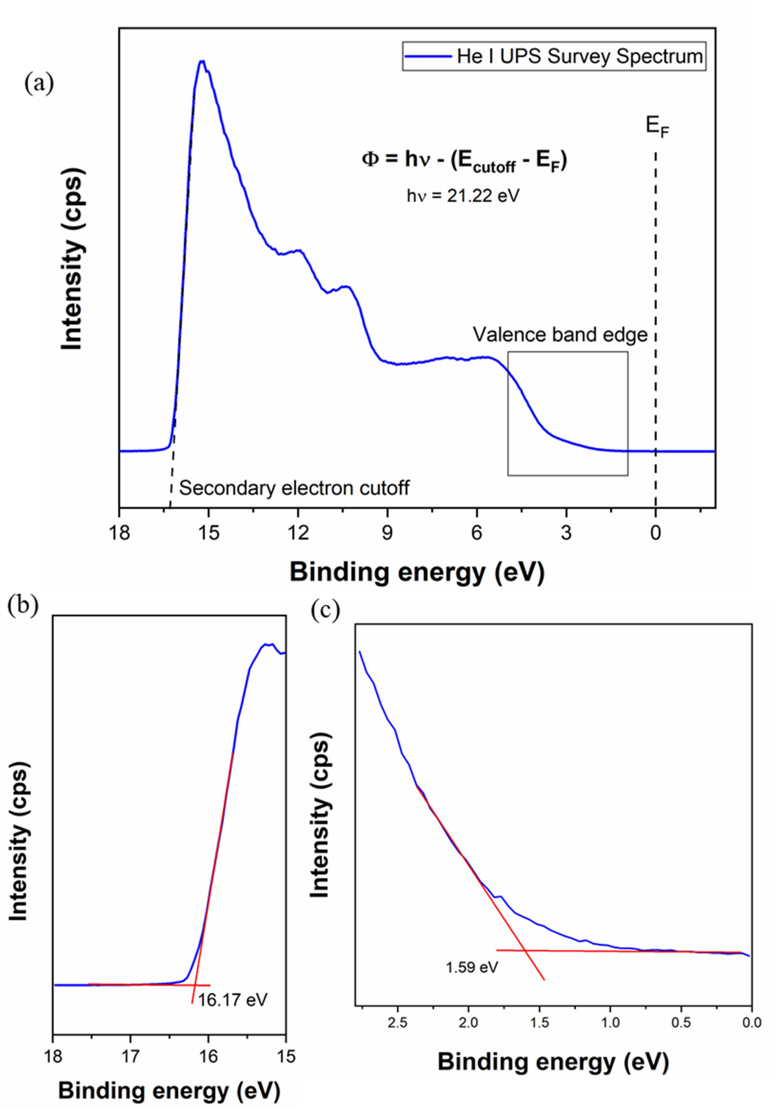

Figure 3.13. *(a) UPS survey spectrum, (b) Secondary electron cutoff region and (c) Valence band edge of CCSC MCs measured using He I radiation.*

An energy level diagram of CCSC MCs was constructed as shown in Figure 3.14, using the bandgap value as determined from the Tauc plot and the VBM and Fermi level as obtained from the UPS spectra. Values of various energy levels have been tabulated in Table 3.2.

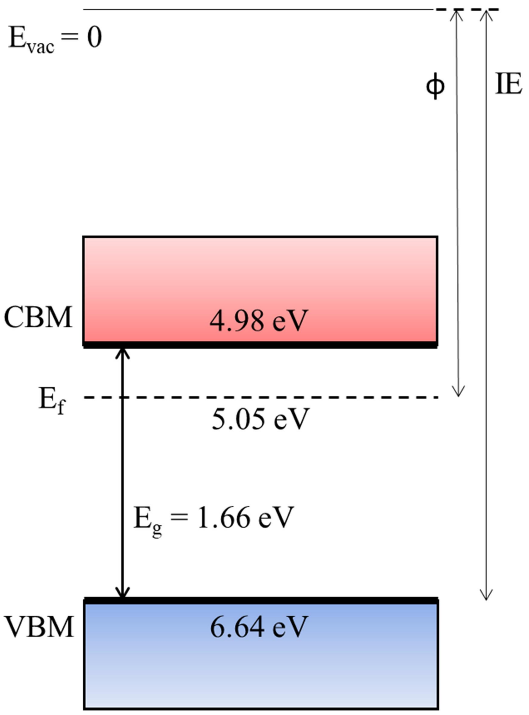

Figure 3.14. *Energy level diagram of CCSC MCs.*

E_{cutoff} (eV)	E_{onset} (eV)	Φ (eV)	VBM (eV)	E_g (eV)	CBM (eV)
16.17	1.59	5.05	6.64	1.66	4.98

Table 3.2. *Energy levels of CCSC MCs as obtained from the UPS spectra and the Tauc plot.*

3.4.9. Femtosecond transient absorption spectroscopy

To understand the intrinsic dynamics in CCSC MCs, femtosecond transient absorption spectroscopy was performed using a 400 nm pump pulse and a white light probe. Figure 3.15 shows the contour plots of the excited state dynamics of CCSC MCs in toluene at short and long time delay, along with the spectral traces at long time delay. A broad ESA signal is predominantly obtained which is centred at 587 nm. The signal rises till 50 ps and decays after that.

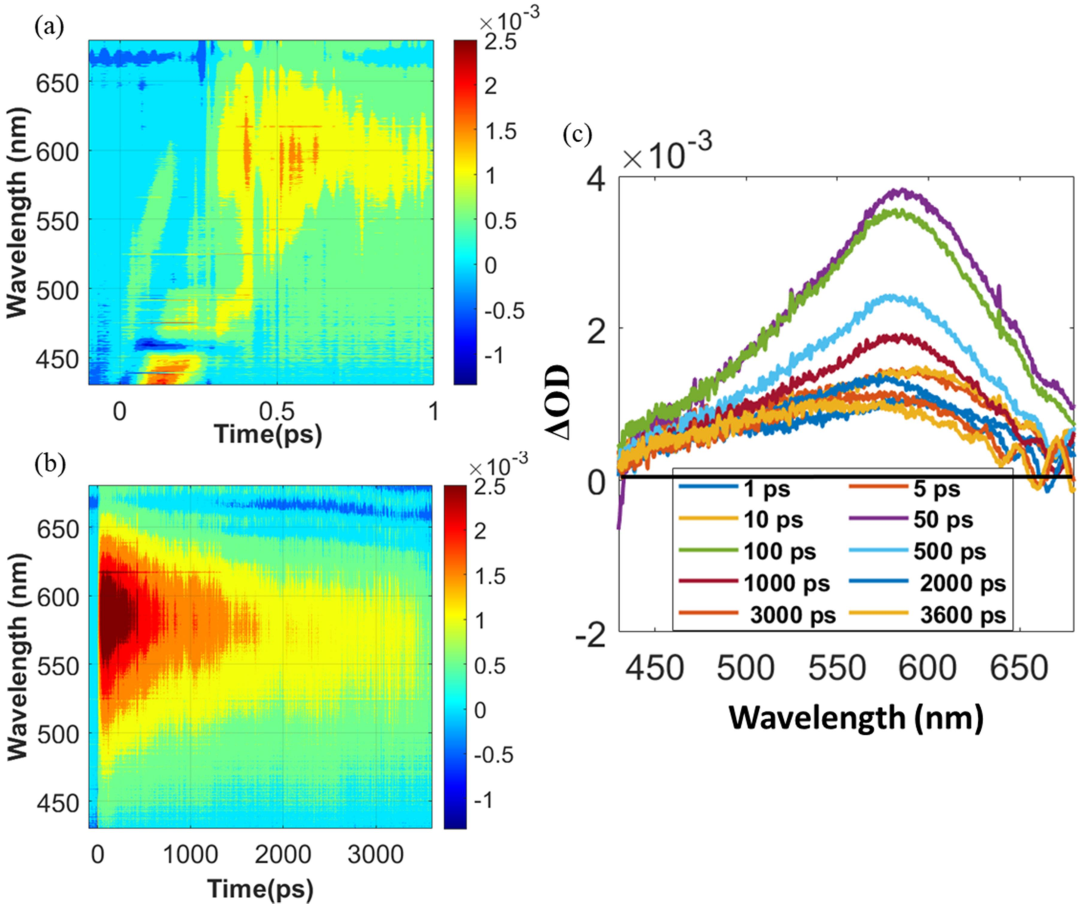

Figure 3.15. *(a) Contour plot of CCSC MCs in toluene at short time delay, (b) Contour plot of CCSC MCs in toluene at long time delay and (c) Spectral traces of CCSC MCs in toluene at long time delay (till 3600 ps).*

Similarly, Figure 3.16 depicts the excited state dynamics of CCSC MCs in chlorobenzene. At short time delay (Figure 3.16 (a)), a strong artefact and a weak signal is observed. These weak signals have been obtained due to the poor signal to noise ratio as can also be seen through the spectral traces where the ESA signal dominates (Figure 3.16 (c)). A rise in the signal is obtained till 50 ps after which it decays.

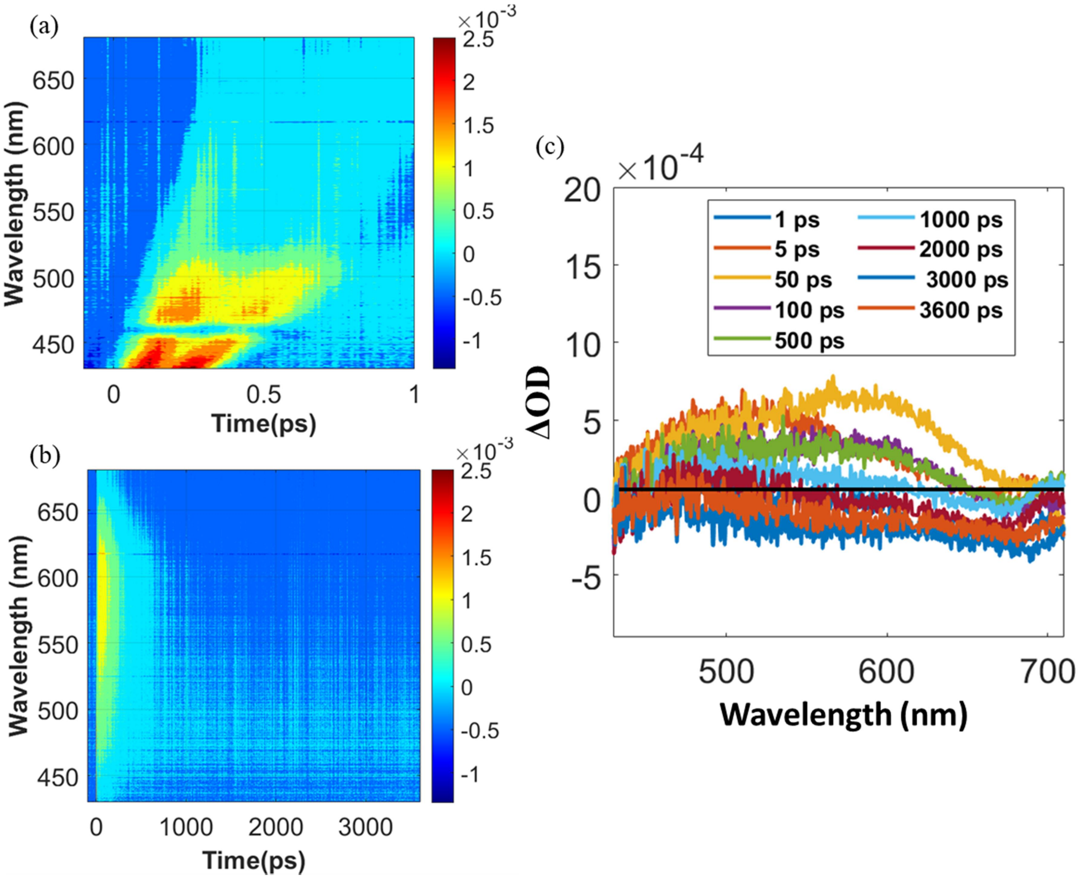

Figure 3.16. *(a) Contour plot of CCSC MCs in chlorobenzene at short time delay, (b) Contour plot of CCSC MCs in chlorobenzene at long time delay and (c) Spectral traces of CCSC MCs in chlorobenzene at long time delay (till 3600 ps).*

The time traces of CCSC obtained at 587 nm (ESA) in toluene and chlorobenzene is shown in Figure 3.17. The time constants and their corresponding amplitudes have been tabulated in Table 3.3. The short time component corresponds to the hot carrier relaxation process, which has been obtained at 274 ps for CCSC in toluene and 67 ps for CCSC in chlorobenzene. This relatively long lifetime supports the use of CCSC as an absorber layer for developing HCSCs. The long time component, on the other hand, corresponds to the trap-assisted recombination process, which has a timescale of about 4 ns in case of CCSC in toluene and 0.8 ns for CCSC in chlorobenzene.

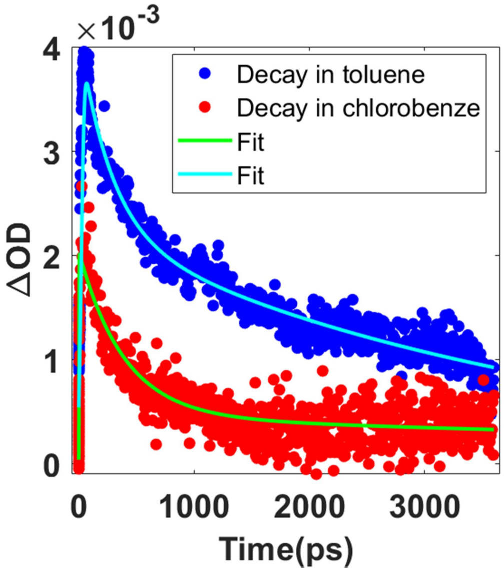

Figure 3.17. *Kinetic traces of CCSC MCs at 587 nm (ESA) in (a) toluene (blue data points) and (b) chlorobenzene (red data points).*

587 nm (ESA)	**α_1**	**τ_1 (ps)**	**α_2**	**τ_2 (ps)**	**σ**	**R^2**
CCSC in Toluene	0.5	274	9.1	4012	11.7	0.93
CCSC in Chlorobenzene	0.6	67	4.5	769	1.2	0.88

Table 3.3. *Time-constants for relaxation dynamics and related amplitudes of CCSC MCs.*

3.5. Conclusion

Microcrystals of CCSC were synthesised and characterised using several experimental techniques. The microcrystals obtained were in irregular in shape and in the submicron range. The material was stable under ambient conditions and formed colloidal solutions in chlorobenzene and toluene. An indirect bandgap of 1.66 eV was obtained as the lowest energy transition for the as-synthesised CCSC MCs. The valence and conduction band levels in CCSC were determined using the UPS technique and tauc plot. Using femtosecond transient absorption spectroscopy, a slow hot carrier relaxation process was observed in the material. This study determines the potential in CCSC to be used as an absorber layer in hot carrier solar cells.

4. Bibliography

(1) Energy Mix. https://en.wikipedia.org/wiki/Energy_mix#/media/File:Total_World_Energy_Consumption_by_Source_2010.png (accessed March 10, 2021).

(2) Energy Sources. https://www.coursera.org/learn/solar-cells/supplement/WmeF4/energy-sources (accessed Mar 10, 2021).

(3) Ewing, R. C. Long-Term Storage of Spent Nuclear Fuel. *Nat. Mater.* **2015**, *14* (3), 252–257.

(4) Available energy. https://www.coursera.org/learn/solar-cells/supplement/zbxPw/available-energy (accessed March 12, 2021).

(5) Renewable Energy. https://en.wikipedia.org/wiki/Renewable_energy (accessed March 12, 2021).

(6) Kabir, E.; Kumar, P.; Kumar, S.; Adelodun, A. A.; Kim, K.-H. Solar Energy: Potential and Future Prospects. *Renew. Sustain. Energy Rev.* **2018**, *82*, 894–900.

(7) Solar Cell History. https://www.coursera.org/learn/solar-cells/supplement/AZK20/solar-cell-history (accessed March 12, 2021).

(8) Copeland, A. W.; Black, O. D.; Garrett, A. B. The Photovoltaic Effect. *Chem. Rev.* **1942**, *31* (1), 177–226.

(9) Fritts, C. E. On a New Form of Selenium Cell, and Some Electrical Discoveries Made by Its Use. *Am. J. Sci.* **1883**, *s3-26* (156), 465–472.

(10) Chapin, D. M.; Fuller, C. S.; Pearson, G. L. A New Silicon P-n Junction Photocell for Converting Solar Radiation into Electrical Power. *J. Appl. Phys.* **1954**, *25* (5), 676–677.

(11) Alferov, Z. I. The History and Future of Semiconductor Heterostructures. *Semiconductors* **1998**, *32* (1), 1–14.

(12) Shockley, W.; Queisser, H. J. Detailed Balance Limit of Efficiency of P-n Junction Solar Cells. *J. Appl. Phys.* **1961**, *32* (3), 510–519.

(13) Rühle, S. Tabulated Values of the Shockley–Queisser Limit for Single Junction Solar Cells. *Sol. Energy* **2016**, *130*, 139–147.

(14) El Chaar, L.; Lamont, L. A.; El Zein, N. Review of Photovoltaic Technologies. *Renew. Sustain. Energy Rev.* **2011**, *15* (5), 2165–2175.

(15) National Renewable Energy Laboratory. Best Research Cell Efficiencies. https://www.nrel.gov/pv/cell-efficiency.html (accessed March 20, 2021).

(16) Blakers, A.; Zin, N.; McIntosh, K. R.; Fong, K. High Efficiency Silicon Solar Cells. *Energy Procedia* **2013**, *33*, 1–10.

(17) Lee, C. H.; Kim, D. R.; Cho, I. S.; William, N.; Wang, Q.; Zheng, X. Peel-and-Stick: Fabricating Thin Film Solar Cell on Universal Substrates. *Sci. Rep.* **2012**, *2* (1), 1000.

(18) Britt, J.; Ferekides, C. Thin-film CdS/CdTe Solar Cell with 15.8% Efficiency. *Appl. Phys. Lett.* **1993**, *62* (22), 2851–2852.

(19) Moon, S.; Kim, K.; Kim, Y.; Heo, J.; Lee, J. Highly Efficient Single-Junction GaAs Thin-Film Solar Cell on Flexible Substrate. *Sci. Rep.* **2016**, *6* (1), 30107.

(20) Conibeer, G. Third-Generation Photovoltaics. *Mater. Today* **2007**, *10* (11), 42–50.

(21) Yan, J.; Saunders, B. R. Third-Generation Solar Cells: A Review and Comparison of Polymer:Fullerene, Hybrid Polymer and Perovskite Solar Cells. *RSC Adv.* **2014**, *4* (82), 43286–43314.

(22) Tanabe, K. A Review of Ultrahigh Efficiency III-V Semiconductor Compound Solar Cells: Multijunction Tandem, Lower Dimensional, Photonic Up/Down Conversion and Plasmonic Nanometallic Structures. *Energies* **2009**, *2* (3), 504–530.

(23) Geisz, J. F.; France, R. M.; Schulte, K. L.; Steiner, M. A.; Norman, A. G.; Guthrey, H. L.; Young, M. R.; Song, T.; Moriarty, T. Six-Junction III–V Solar Cells with 47.1% Conversion Efficiency under 143 Suns Concentration. *Nat. Energy* **2020**, *5* (4), 326–335.

(24) Kojima, A.; Teshima, K.; Shirai, Y.; Miyasaka, T. Organometal Halide Perovskites

as Visible-Light Sensitizers for Photovoltaic Cells. *J. Am. Chem. Soc.* **2009**, *131* (17), 6050–6051.

(25) Leo, K. Signs of Stability. *Nat. Nanotechnol.* **2015**, *10* (7), 574–575.

(26) Lee, M. M.; Teuscher, J.; Miyasaka, T.; Murakami, T. N.; Snaith, H. J. Efficient Hybrid Solar Cells Based on Meso-Superstructured Organometal Halide Perovskites. *Science* **2012**, *338* (6107), 643–647.

(27) Rose, G. Beschreibung Einiger Neuen Mineralien Des Urals. *Ann. der Phys. und Chemie* **1839**, *124* (12), 551–573.

(28) Green, M. A.; Ho-Baillie, A.; Snaith, H. J. The Emergence of Perovskite Solar Cells. *Nat. Photonics* **2014**, *8* (7), 506–514.

(29) Stranks, S. D.; Snaith, H. J. Metal-Halide Perovskites for Photovoltaic and Light-Emitting Devices. *Nat. Nanotechnol.* **2015**, *10* (5), 391–402.

(30) Yi, Z.; Ladi, N. H.; Shai, X.; Li, H.; Shen, Y.; Wang, M. Will Organic–Inorganic Hybrid Halide Lead Perovskites Be Eliminated from Optoelectronic Applications? *Nanoscale Adv.* **2019**, *1* (4), 1276–1289.

(31) Ahn, N.; Son, D. Y.; Jang, I. H.; Kang, S. M.; Choi, M.; Park, N. G. Highly Reproducible Perovskite Solar Cells with Average Efficiency of 18.3% and Best Efficiency of 19.7% Fabricated via Lewis Base Adduct of Lead(II) Iodide. *J. Am. Chem. Soc.* **2015**, *137* (27), 8696–8699.

(32) Brenner, T. M.; Egger, D. A.; Kronik, L.; Hodes, G.; Cahen, D. Hybrid Organic - Inorganic Perovskites: Low-Cost Semiconductors with Intriguing Charge-Transport Properties. *Nat. Rev. Mater.* **2016**, *1* (1).

(33) Weller, M. T.; Weber, O. J.; Henry, P. F.; Di Pumpo, A. M.; Hansen, T. C. Complete Structure and Cation Orientation in the Perovskite Photovoltaic Methylammonium Lead Iodide between 100 and 352 K. *Chem. Commun.* **2015**, *51* (20), 4180–4183.

(34) De Wolf, S.; Holovsky, J.; Moon, S. J.; Löper, P.; Niesen, B.; Ledinsky, M.; Haug, F. J.; Yum, J. H.; Ballif, C. Organometallic Halide Perovskites: Sharp Optical Absorption Edge and Its Relation to Photovoltaic Performance. *J. Phys. Chem.*

Lett. **2014**, *5* (6), 1035–1039.

(35) Butler, K. T.; Frost, J. M.; Walsh, A. Band Alignment of the Hybrid Halide Perovskites $CH_3NH_3PbCl_3$, $CH_3NH_3PbBr_3$ and $CH_3NH_3PbI_3$. *Mater. Horizons* **2015**, *2* (2), 228–231.

(36) Protesescu, L.; Yakunin, S.; Bodnarchuk, M. I.; Krieg, F.; Caputo, R.; Hendon, C. H.; Yang, R. X.; Walsh, A.; Kovalenko, M. V. Nanocrystals of Cesium Lead Halide Perovskites ($CsPbX_3$, X = Cl, Br, and I): Novel Optoelectronic Materials Showing Bright Emission with Wide Color Gamut. *Nano Lett.* **2015**, *15* (6), 3692–3696.

(37) Tan, Z. K.; Moghaddam, R. S.; Lai, M. L.; Docampo, P.; Higler, R.; Deschler, F.; Price, M.; Sadhanala, A.; Pazos, L. M.; Credgington, D.; Hanusch, F.; Bein, T.; Snaith, H. J.; Friend, R. H. Bright Light-Emitting Diodes Based on Organometal Halide Perovskite. *Nat. Nanotechnol.* **2014**, *9* (9), 687–692.

(38) Manser, J. S.; Kamat, P. V. Band Filling with Free Charge Carriers in Organometal Halide Perovskites. *Nat. Photonics* **2014**, *8* (9), 737–743.

(39) Hutter, E. M.; Eperon, G. E.; Stranks, S. D.; Savenije, T. J. Charge Carriers in Planar and Meso-Structured Organic–Inorganic Perovskites: Mobilities, Lifetimes, and Concentrations of Trap States. *J. Phys. Chem. Lett.* **2015**, *6* (15), 3082–3090.

(40) Oga, H.; Saeki, A.; Ogomi, Y.; Hayase, S.; Seki, S. Improved Understanding of the Electronic and Energetic Landscapes of Perovskite Solar Cells: High Local Charge Carrier Mobility, Reduced Recombination, and Extremely Shallow Traps. *J. Am. Chem. Soc.* **2014**, *136* (39), 13818–13825.

(41) Wehrenfennig, C.; Eperon, G. E.; Johnston, M. B.; Snaith, H. J.; Herz, L. M. High Charge Carrier Mobilities and Lifetimes in Organolead Trihalide Perovskites. *Adv. Mater.* **2014**, *26* (10), 1584–1589.

(42) Zhu, X.-Y.; Podzorov, V. Charge Carriers in Hybrid Organic–Inorganic Lead Halide Perovskites Might Be Protected as Large Polarons. *J. Phys. Chem. Lett.* **2015**, *6* (23), 4758–4761.

(43) Shi, D.; Adinolfi, V.; Comin, R.; Yuan, M.; Alarousu, E.; Buin, A.; Chen, Y.;

Hoogland, S.; Rothenberger, A.; Katsiev, K.; Losovyj, Y.; Zhang, X.; Dowben, P. A.; Mohammed, O. F.; Sargent, E. H.; Bakr, O. M. Low Trap-State Density and Long Carrier Diffusion in Organolead Trihalide Perovskite Single Crystals. *Science (80-.).* **2015**, *347* (6221), 519–522.

(44) Yin, W. J.; Shi, T.; Yan, Y. Superior Photovoltaic Properties of Lead Halide Perovskites: Insights from First-Principles Theory. *J. Phys. Chem. C* **2015**, *119* (10), 5253–5264.

(45) Emami, S.; Andrade, L.; Mendes, A. Recent Progress in Long-Term Stability of Perovskite Solar Cells. *U.Porto J. Eng.* **2018**, *1* (2), 52–62.

(46) Perovskite Solar Cells: Causes of Degradation. https://www.ossila.com/pages/perovskite-solar-cell-degradation-causes (accessed March 17, 2021).

(47) Rajagopal, A.; Yao, K.; Jen, A. K.-Y. Toward Perovskite Solar Cell Commercialization: A Perspective and Research Roadmap Based on Interfacial Engineering. *Adv. Mater.* **2018**, *30* (32), 1800455.

(48) Conings, B.; Drijkoningen, J.; Gauquelin, N.; Babayigit, A.; D'Haen, J.; D'Olieslaeger, L.; Ethirajan, A.; Verbeeck, J.; Manca, J.; Mosconi, E.; Angelis, F. De; Boyen, H.-G. Intrinsic Thermal Instability of Methylammonium Lead Trihalide Perovskite. *Adv. Energy Mater.* **2015**, *5* (15), 1500477.

(49) Philippe, B.; Park, B.-W.; Lindblad, R.; Oscarsson, J.; Ahmadi, S.; Johansson, E. M. J.; Rensmo, H. Chemical and Electronic Structure Characterization of Lead Halide Perovskites and Stability Behavior under Different Exposures—A Photoelectron Spectroscopy Investigation. *Chem. Mater.* **2015**, *27* (5), 1720–1731.

(50) Azpiroz, J. M.; Mosconi, E.; Bisquert, J.; De Angelis, F. Defect Migration in Methylammonium Lead Iodide and Its Role in Perovskite Solar Cell Operation. *Energy Environ. Sci.* **2015**, *8* (7), 2118–2127.

(51) Perovskite Solar Cells: Methods of Increasing Stability & Durability. https://www.ossila.com/pages/perovskite-solar-cells-methods-increase-stability (accessed March 20, 2021).

(52) Gevorgyan, S. A.; Madsen, M. V.; Dam, H. F.; Jørgensen, M.; Fell, C. J.; Anderson, K. F.; Duck, B. C.; Mescheloff, A.; Katz, E. A.; Elschner, A.; Roesch, R.; Hoppe, H.; Hermenau, M.; Riede, M.; Krebs, F. C. Interlaboratory Outdoor Stability Studies of Flexible Roll-to-Roll Coated Organic Photovoltaic Modules: Stability over 10,000h. *Sol. Energy Mater. Sol. Cells* **2013**, *116*, 187–196.

(53) Bella, F.; Griffini, G.; Correa-Baena, J.-P.; Saracco, G.; Gratzel, M.; Hagfeldt, A.; Turri, S.; Gerbaldi, C. Improving Efficiency and Stability of Perovskite Solar Cells with Photocurable Fluoropolymers. *Science).* **2016**, *354* (6309), 203–206.

(54) Wang, D.; Wright, M.; Elumalai, N. K.; Uddin, A. Stability of Perovskite Solar Cells. *Sol. Energy Mater. Sol. Cells* **2016**, *147*, 255–275.

(55) Kulbak, M.; Cahen, D.; Hodes, G. How Important Is the Organic Part of Lead Halide Perovskite Photovoltaic Cells? Efficient $CsPbBr_3$ Cells. *J. Phys. Chem. Lett.* **2015**, *6* (13), 2452–2456.

(56) Hao, F.; Stoumpos, C. C.; Cao, D. H.; Chang, R. P. H.; Kanatzidis, M. G. Lead-Free Solid-State Organic–Inorganic Halide Perovskite Solar Cells. *Nat. Photonics* **2014**, *8* (6), 489–494.

(57) Noel, N. K.; Stranks, S. D.; Abate, A.; Wehrenfennig, C.; Guarnera, S.; Haghighirad, A.-A.; Sadhanala, A.; Eperon, G. E.; Pathak, S. K.; Johnston, M. B.; Petrozza, A.; Herz, L. M.; Snaith, H. J. Lead-Free Organic–Inorganic Tin Halide Perovskites for Photovoltaic Applications. *Energy Environ. Sci.* **2014**, *7* (9), 3061–3068.

(58) Stoumpos, C. C.; Frazer, L.; Clark, D. J.; Kim, Y. S.; Rhim, S. H.; Freeman, A. J.; Ketterson, J. B.; Jang, J. I.; Kanatzidis, M. G. Hybrid Germanium Iodide Perovskite Semiconductors: Active Lone Pairs, Structural Distortions, Direct and Indirect Energy Gaps, and Strong Nonlinear Optical Properties. *J. Am. Chem. Soc.* **2015**, *137* (21), 6804–6819.

(59) Maughan, A. E.; Ganose, A. M.; Bordelon, M. M.; Miller, E. M.; Scanlon, D. O.; Neilson, J. R. Defect Tolerance to Intolerance in the Vacancy-Ordered Double Perovskite Semiconductors Cs_2SnI_6 and Cs_2TeI_6. *J. Am. Chem. Soc.* **2016**, *138* (27), 8453–8464.

(60) Giustino, F.; Snaith, H. J. Toward Lead-Free Perovskite Solar Cells. *ACS Energy Lett.* **2016**, *1* (6), 1233–1240.

(61) Saparov, B.; Hong, F.; Sun, J.-P.; Duan, H.-S.; Meng, W.; Cameron, S.; Hill, I. G.; Yan, Y.; Mitzi, D. B. Thin-Film Preparation and Characterization of $Cs_3Sb_2I_9$: A Lead-Free Layered Perovskite Semiconductor. *Chem. Mater.* **2015**, *27* (16), 5622–5632.

(62) Zhang, L.; Wang, K.; Zou, B. Bismuth Halide Perovskite-Like Materials: Current Opportunities and Challenges. *ChemSusChem* **2019**, *12* (8), 1612–1630.

(63) Pal, J.; Manna, S.; Mondal, A.; Das, S.; Adarsh, K. V.; Nag, A. Colloidal Synthesis and Photophysics of $M_3Sb_2I_9$ (M=Cs and Rb) Nanocrystals: Lead-Free Perovskites. *Angew. Chemie Int. Ed.* **2017**, *56* (45), 14187–14191.

(64) Creutz, S. E.; Crites, E. N.; De Siena, M. C.; Gamelin, D. R. Colloidal Nanocrystals of Lead-Free Double-Perovskite (Elpasolite) Semiconductors: Synthesis and Anion Exchange To Access New Materials. *Nano Lett.* **2018**, *18* (2), 1118–1123.

(65) Slavney, A. H.; Hu, T.; Lindenberg, A. M.; Karunadasa, H. I. A Bismuth-Halide Double Perovskite with Long Carrier Recombination Lifetime for Photovoltaic Applications. *J. Am. Chem. Soc.* **2016**, *138* (7), 2138–2141.

(66) McClure, E. T.; Ball, M. R.; Windl, W.; Woodward, P. M. Cs_2AgBiX_6 (X = Br, Cl): New Visible Light Absorbing, Lead-Free Halide Perovskite Semiconductors. *Chem. Mater.* **2016**, *28* (5), 1348–1354.

(67) Xiao, Z.; Du, K.-Z.; Meng, W.; Wang, J.; Mitzi, D. B.; Yan, Y. Intrinsic Instability of $Cs_2In(I)M(III)X_6$ (M = Bi, Sb; X = Halogen) Double Perovskites: A Combined Density Functional Theory and Experimental Study. *J. Am. Chem. Soc.* **2017**, *139* (17), 6054–6057.

(68) Hoefler, S. F.; Trimmel, G.; Rath, T. Progress on Lead-Free Metal Halide Perovskites for Photovoltaic Applications: A Review. *Monatshefte für Chemie - Chem. Mon.* **2017**, *148* (5), 795–826.

(69) Tang, G.; Xiao, Z.; Hosono, H.; Kamiya, T.; Fang, D.; Hong, J. Layered Halide

Double Perovskites $Cs_{3+n}M(II)_nSb_2X_{9+3n}$ (M = Sn, Ge) for Photovoltaic Applications. *J. Phys. Chem. Lett.* **2018**, *9* (1), 43–48.

(70) Vargas, B.; Torres-Cadena, R.; Reyes-Castillo, D. T.; Rodríguez-Hernández, J.; Gembicky, M.; Menéndez-Proupin, E.; Solis-Ibarra, D. Chemical Diversity in Lead-Free, Layered Double Perovskites: A Combined Experimental and Computational Approach. *Chem. Mater.* **2020**, *32* (1), 424–429.

(71) Liu, M.; Johnston, M. B.; Snaith, H. J. Efficient Planar Heterojunction Perovskite Solar Cells by Vapour Deposition. *Nature* **2013**, *501* (7467), 395–398.

(72) Ball, J. M.; Lee, M. M.; Hey, A.; Snaith, H. J. Low-Temperature Processed Meso-Superstructured to Thin-Film Perovskite Solar Cells. *Energy Environ. Sci.* **2013**, *6* (6), 1739.

(73) Mishra, S.; Takhellambam, D.; De, A. K.; Jana, D. Stable $CsPbI_3$ -Mesoporous Alumina Composite Thin Film at Ambient Condition: Preparation, Characterization, and Study of Ultrafast Charge-Transfer Dynamics . *J. Phys. Chem. C* **2021**, 1–19.

(74) Zhou, D.; Zhou, T.; Tian, Y.; Zhu, X.; Tu, Y. Perovskite-Based Solar Cells: Materials, Methods, and Future Perspectives. *J. Nanomater.* **2018**.

(75) Herz, L. M. Charge-Carrier Dynamics in Organic-Inorganic Metal Halide Perovskites. *Annu. Rev. Phys. Chem.* **2016**, *67*, 65–89.

(76) Auger Effect in Semiconductors. *Proc. R. Soc. London. Ser. A. Math. Phys. Sci.* **1959**, *249* (1256), 16–29.

(77) Zhou, H.; Chen, Q.; Li, G.; Luo, S.; Song, T. -b.; Duan, H.-S.; Hong, Z.; You, J.; Liu, Y.; Yang, Y. Interface Engineering of Highly Efficient Perovskite Solar Cells. *Science (80-.).* **2014**, *345* (6196), 542–546.

(78) Li, M.; Fu, J.; Xu, Q.; Sum, T. C. Slow Hot-Carrier Cooling in Halide Perovskites: Prospects for Hot-Carrier Solar Cells. *Adv. Mater.* **2019**, *31* (47), 1802486.

(79) König, D.; Casalenuovo, K.; Takeda, Y.; Conibeer, G.; Guillemoles, J. F.; Patterson, R.; Huang, L. M.; Green, M. A. Hot Carrier Solar Cells: Principles, Materials and Design. *Phys. E Low-dimensional Syst. Nanostructures* **2010**, *42*

(10), 2862–2866.

(80) Ross, R. T.; Nozik, A. J. Efficiency of Hot-carrier Solar Energy Converters. *J. Appl. Phys.* **1982**, *53* (5), 3813–3818.

(81) Xing, G.; Mathews, N.; Sun, S.; Lim, S. S.; Lam, Y. M.; Gratzel, M.; Mhaisalkar, S.; Sum, T. C. Long-Range Balanced Electron- and Hole-Transport Lengths in Organic-Inorganic CH3NH3PbI3. *Science* **2013**, *342* (6156), 344–347.

(82) Sum, T. C.; Mathews, N.; Xing, G.; Lim, S. S.; Chong, W. K.; Giovanni, D.; Dewi, H. A. Spectral Features and Charge Dynamics of Lead Halide Perovskites: Origins and Interpretations. *Acc. Chem. Res.* **2016**, *49* (2), 294–302.

(83) Chen, K.; Barker, A. J.; Morgan, F. L. C.; Halpert, J. E.; Hodgkiss, J. M. Effect of Carrier Thermalization Dynamics on Light Emission and Amplification in Organometal Halide Perovskites. *J. Phys. Chem. Lett.* **2015**, *6* (1), 153–158.

(84) Yang, Y.; Ostrowski, D. P.; France, R. M.; Zhu, K.; van de Lagemaat, J.; Luther, J. M.; Beard, M. C. Observation of a Hot-Phonon Bottleneck in Lead-Iodide Perovskites. *Nat. Photonics* **2016**, *10* (1), 53–59.

(85) Yang, J.; Wen, X.; Xia, H.; Sheng, R.; Ma, Q.; Kim, J.; Tapping, P.; Harada, T.; Kee, T. W.; Huang, F.; Cheng, Y.-B.; Green, M.; Ho-Baillie, A.; Huang, S.; Shrestha, S.; Patterson, R.; Conibeer, G. Acoustic-Optical Phonon up-Conversion and Hot-Phonon Bottleneck in Lead-Halide Perovskites. *Nat. Commun.* **2017**, *8* (1), 14120.

(86) Park, M.; Neukirch, A. J.; Reyes-Lillo, S. E.; Lai, M.; Ellis, S. R.; Dietze, D.; Neaton, J. B.; Yang, P.; Tretiak, S.; Mathies, R. A. Excited-State Vibrational Dynamics toward the Polaron in Methylammonium Lead Iodide Perovskite. *Nat. Commun.* **2018**, *9* (1), 2525.

(87) Prabhu, S. S.; Vengurlekar, A. S.; Roy, S. K.; Shah, J. Nonequilibrium Dynamics of Hot Carriers and Hot Phonons in CdSe and GaAs. *Phys. Rev. B* **1995**, *51* (20), 14233–14246.

(88) Caretta, A.; Donker, M. C.; Perdok, D. W.; Abbaszadeh, D.; Polyakov, A. O.; Havenith, R. W. A.; Palstra, T. T. M.; van Loosdrecht, P. H. M. Measurement of

the Acoustic-to-Optical Phonon Coupling in Multicomponent Systems. *Phys. Rev. B* **2015**, *91* (5), 054111.

(89) Fu, J.; Xu, Q.; Han, G.; Wu, B.; Huan, C. H. A.; Leek, M. L.; Sum, T. C. Hot Carrier Cooling Mechanisms in Halide Perovskites. *Nat. Commun.* **2017**, *8* (1), 1300.

(90) Zhu, H.; Miyata, K.; Fu, Y.; Wang, J.; Joshi, P. P.; Niesner, D.; Williams, K. W.; Jin, S.; Zhu, X.-Y. Screening in Crystalline Liquids Protects Energetic Carriers in Hybrid Perovskites. *Science* **2016**, *353* (6306), 1409–1413.

(91) Fang, H.-H.; Adjokatse, S.; Shao, S.; Even, J.; Loi, M. A. Long-Lived Hot-Carrier Light Emission and Large Blue Shift in Formamidinium Tin Triiodide Perovskites. *Nat. Commun.* **2018**, *9* (1), 243.

(92) Hopper, T. R.; Gorodetsky, A.; Frost, J. M.; Müller, C.; Lovrincic, R.; Bakulin, A. A. Ultrafast Intraband Spectroscopy of Hot-Carrier Cooling in Lead-Halide Perovskites. *ACS Energy Lett.* **2018**, *3* (9), 2199–2205.

(93) Hedley, G. J.; Quarti, C.; Harwell, J.; Prezhdo, O. V.; Beljonne, D.; Samuel, I. D. W. Hot-Hole Cooling Controls the Initial Ultrafast Relaxation in Methylammonium Lead Iodide Perovskite. *Sci. Rep.* **2018**, *8* (1), 8115.

(94) Yang, B.; Chen, J.; Yang, S.; Hong, F.; Sun, L.; Han, P.; Pullerits, T.; Deng, W.; Han, K. Lead-Free Silver-Bismuth Halide Double Perovskite Nanocrystals. *Angew. Chemie* **2018**, *130* (19), 5457–5461.

(95) Guo, Z.; Wan, Y.; Yang, M.; Snaider, J.; Zhu, K.; Huang, L. Long-Range Hot-Carrier Transport in Hybrid Perovskites Visualized by Ultrafast Microscopy. *Science (80-.).* **2017**, *356* (6333), 59–62.

(96) Shen, Q.; Ripolles, T. S.; Even, J.; Ogomi, Y.; Nishinaka, K.; Izuishi, T.; Nakazawa, N.; Zhang, Y.; Ding, C.; Liu, F.; Toyoda, T.; Yoshino, K.; Minemoto, T.; Katayama, K.; Hayase, S. Slow Hot Carrier Cooling in Cesium Lead Iodide Perovskites. *Appl. Phys. Lett.* **2017**, *111* (15), 153903.

(97) Sarkar, S.; Ravi, V. K.; Banerjee, S.; Yettapu, G. R.; Markad, G. B.; Nag, A.; Mandal, P. Terahertz Spectroscopic Probe of Hot Electron and Hole Transfer from

Colloidal $CsPbBr_3$ Perovskite Nanocrystals. *Nano Lett.* **2017**, *17* (9), 5402–5407.

(98) Conibeer, G. J.; Jiang, C.-W.; König, D.; Shrestha, S.; Walsh, T.; Green, M. A. Selective Energy Contacts for Hot Carrier Solar Cells. *Thin Solid Films* **2008**, *516* (20), 6968–6973.

(99) Vargas, B.; Ramos, E.; Pérez-Gutiérrez, E.; Alonso, J. C.; Solis-Ibarra, D. A Direct Bandgap Copper-Antimony Halide Perovskite. *J. Am. Chem. Soc.* **2017**, *139* (27), 9116–9119.

(100) Cai, T.; Shi, W.; Hwang, S.; Kobbekaduwa, K.; Nagaoka, Y.; Yang, H.; Hills-Kimball, K.; Zhu, H.; Wang, J.; Wang, Z.; Liu, Y.; Su, D.; Gao, J.; Chen, O. Lead-Free $Cs_4CuSb_2Cl_{12}$ Layered Double Perovskite Nanocrystals. *J. Am. Chem. Soc.* **2020**, *142* (27), 11927–11936.

(101) Singhal, N.; Chakraborty, R.; Ghosh, P.; Nag, A. Low-Bandgap $Cs_4CuSb_2Cl_{12}$ Layered Double Perovskite: Synthesis, Reversible Thermal Changes, and Magnetic Interaction. *Chem. - An Asian J.* **2018**, *13* (16), 2085–2092.

(102) Jayasankar, P. M.; Pathak, A. K.; Madhusudanan, S. P.; Murali, S.; Batabyal, S. K. Double Perovskite $Cs_4CuSb_2Cl_{12}$ Microcrystalline Device for Cost Effective Photodetector Applications. *Mater. Lett.* **2020**, *263*, 127200.

(103) Wang, X. D.; Miao, N. H.; Liao, J. F.; Li, W. Q.; Xie, Y.; Chen, J.; Sun, Z. M.; Chen, H. Y.; Kuang, D. Bin. The Top-down Synthesis of Single-Layered $Cs_4CuSb_2Cl_{12}$ Halide Perovskite Nanocrystals for Photoelectrochemical Application. *Nanoscale* **2019**, *11* (12), 5180–5187.

(104) Wang, X.; Meng, W.; Xiao, Z.; Wang, J.; Mitzi, D.; Yan, Y. First-Principles Understanding of the Electronic Band Structure of Copper-Antimony Halide Perovskite: The Effect of Magnetic Ordering. *arXiv* **2017**, *1* (d), 1–8.

(105) Perdew, J. P.; Burke, K.; Ernzerhof, M. Generalized Gradient Approximation Made Simple. *Phys. Rev. Lett.* **1996**, *77* (18), 3865–3868.